Jet Propulsion Laboratory
California Institute of Technology
4800 Oak Grove Drive
Pasadena, California

GCA Technical Report No. 62-17-G

GEOPHYSICS CORPORATION OF AMERICA
Bedford, Massachusetts

FINAL REPORT

R. F. K. Herzog

W. P. Poschenrieder

MASS SPECTROMETER INSTRUMENTATION FOR
THE ANALYSIS OF THE MARTIAN ATMOSPHERE

CONTRACT NO. 950328

FILE 2751B

12 December 1962

TABLE OF CONTENTS

SECTION 1

INTRODUCTION

The ion sources which have been used for mass spectrometers can be divided into two groups:

(1) Mono-energetic sources, where all ions obtain essentially the same energy. Examples are the electron impact source of Nier, thermionic sources and low voltage arc sources as, for instance, the Duoplasmatron. In all these cases a fair resolution can be obtained with a simple mass analyzer consisting of a magnetic field only.

(2) Hetero-energetic sources, which produce ions of largely different energies. Examples are the spark source of Dempster, the gas discharge tube in Aston's instrument or in Mattauch-Herzog's mass spectrograph. These ion sources require a more complex mass analyzer which consists of a magnetic and electric field, the latter one acting as a preselector of ions with energies within a narrow range. Usually velocity focusing is provided in these instruments which results in better resolution and sensitivity. The greater complexity of the deflection fields and the more difficult adjustment are disadvantages of these more sophisticated instruments.

The following paper describes a new mass spectrometer which uses a hetero-energetic ion source without need of any specific deflection field. This instrument is therefore of extreme simplicity and of great value for applications where high reliability, small size, small weight and low power consumption are of prime importance and where a moderate resolution is adequate.

The ion source is of the inverted magnetron type as described by P. Redhead.[1-1] It consists of two electrodes, an anode cylinder which is concentric surrounded by a can-shaped cathode at ground potential. An axial magnetic field confines the electrons in a potential well, thus considerably increasing their ionizing efficiency. The auxiliary cathodes, devised by Redhead, could be omitted in the present setup, since the ion source will be operated at pressures between 10^{-6} - 10^{-4} torr.

The ions are under the influence of a radial electric and axial magnetic field. Orbits in crossed electric and magnetic fields have been investigated by many authors, some of them shall be mentioned here. Bleakney and Hipple[1-2] studied the orbits in crossed homogeneous electric and magnetic fields and discovered their valuable focussing properties. Coggeshall[1-3] extended these calculations to cover inhomogeneous fields of different kinds. However, the formulas became rather complex and the discussion of the results provides only a very limited insight in the ion-optical properties of these fields. Herzog[1-4] discussed nearly circular orbits in a homogeneous magnetic field and a crossed radial electric field and found the ion-optical properties of such a system.

2

The present paper investigates another special kind of orbits which occurs if the magnetic field is weak and the ions follow essentially the straight lines of the electric force. Such conditions exist in the previously mentioned inverse magnetron type discharge. It will be shown that under certain field conditions, velocity focussing can be achieved which permits use of this hetero-energetic ion source as a mass spectrometer. The computations will be carried out first for an axial symmetrical setup since this one was tried first in pursuance of Redhead's work. However, it was soon found that a plane geometry would provide higher resolution and other advantages. This resulted in a setup which is quite different from Redhead's. The computations for this case are presented in the second part of Section 2.

Before going into the details of the calculations, a qualitative description of the phenomena shall be given. Referring to Figure 2-1, the electric field is maintained between the cathode and anode. In the plane of symmetry, which is chosen as the plane of drawing, the electrical field is only in radial direction. However, outside the plane of symmetry, the electrodes are bent and a Z component of the electric field exists. The same is true for the magnetic field which normally intersects the plane of symmetry. Both fields do not have to be homogeneous and their field strength may depend on the r coordinate. An ion which is formed at the point r^* will be first accelerated in the r direction (the direction of the electric field). With increasing velocity the magnetic force in the y direction will increase and deflect the beam.

3

Only particles which have been ionized at very special locations will be able to pass the hole in the cathode. The direction ψ of the orbit when passing through the cathode exit hole depends on the point of ionization r^* and so does the velocity of the ion. If ionization occurs near the cathode, the velocity and deflection ψ are both small. If ionization occurs nearer to the anode the energy becomes larger and so does, in general, the deflection angle ψ until acceleration to high energies tends to reduce the deflection. Therefore, ψ has a maximum for a certain region of ionization and this is the place where the anode should be located. This location of the anode will prevent particles from obtaining energies higher than those for which energy focusing is achieved. Lower energies can be repelled by a retarding field on the ion collector. The energy range which can be focussed this way can be extended by proper choice of the fields; this is one of the main objectives of the following work.

Ionization can occur at any place where the electron energy is larger than the ionization potential of the gas. This electron energy is proportional to $(E/H)^2$ which means that, with increasing voltage, ionization occurs first at the places of highest electric field strength, which are near the anode. However, there may exist a narrow electron free region around the anode from which all electrons are rapidly lost to the edges of the anode. This means that the maximum energy of the ions may be less than the voltage applied to the anode. The magnitude

4

of this effect depends on the shape of anode and cathode, on the inhomo-geneousness of the magnetic field and on the space charge of the electron cloud. The latter one depends on many parameters and can only be deter-mined experimentally as will be shown in Section 5.

REFERENCES

1-1. Redhead, P. A., Can. J. Phys. 36, 255 (1958).

1-2. Bleakney, W. and Hipple, J. A., Phys. Rev, 53, 521 (1938).

1-3. Coggeshall, N. D., Phys. Rev., 70, 270 (1946).

1-4. Herzog, R., Z.f. Phys., 89, 447 (1934).

SECTION 2

ION-ORBITS IN AN INVERSED MAGNETRON GAUGE

2.1 AXIAL SYMMETRY

2.1.1 Deflection in the Main Electromagnetic Field. The gauge

consists basically of two electrodes. The inner electrode or anode is

at

on a positive potential of about 400-3000 V and has a cylindrical,

spherical or any other axial symmetrical shape. This electrode is

completely surrounded by the cathode, which is kept at ground potential.

This electrode too can have any axial symmetrical shape and is placed

coaxial around the anode. The electrostatic field between these

electrodes depends on their shape and on the space charge between them.

Although this field can not be computed accurately it will be between a

spherical and cylindrical field. The following calculations will be

carried out for these special cases.

An axial symmetric magnetic field of about 1000 Gauss is applied in

the axial direction of the electrodes. The intensity of the field

shall be a function of the distance from the axis. It shall be fairly

constant within the cathode and declining rapidly outside.

Neutral gas molecules may be ionized by electron impact at any place within the space between anode and cathode where the electron energy exceeds the ionization energy. The ions have initial energies of a few electron volts and are initially moving in any direction. The electrostatic potential at any point of the field shall be called V, the one at the point where the ionization takes place V^*, and the initial energy of the ions V_o (measured in electron volts). The energy equation provides the total velocity v at any point of the field:

$$v = \sqrt{\frac{2e}{m} (V_o + V^* - V)} \qquad (2\text{-}1)$$

In first approximation we will neglect the initial energy V_o. However, it should be kept in mind that this initial velocity will limit the ultimate resolution of the instrument. The radial velocity $\dot{r}$ is given by

$$\dot{r} = \sqrt{v^2 - r^2 \dot{\phi}^2} \qquad (2\text{-}2)$$

Since for the intended applications the beam deflection will be small, or $r \dot{\phi} \ll v$ we may neglect the second term. This results in

$$\dot{r} = \sqrt{\frac{2e}{m} (V^* - V)} \qquad (2\text{-}3)$$

8

The deflecting force equation in polar coordinates r, φ is given by

$$\frac{m}{r} \frac{d}{dt} (r^2 \dot{\varphi}) = \frac{e}{c} H \cdot \dot{r} \qquad (2\text{-}4)$$

which can be integrated resulting in

$$r^2 \dot{\varphi} = \frac{e}{mc} \int_{r^*}^{r} r \cdot H(r) \, dr \qquad (2\text{-}5)$$

In this equation r^* is the distance between the axis and the point where the angular velocity $\dot{\varphi}$ is zero which is assumed to be the point of ionization. The deflection ψ of the beam against the radial direction is given by

$$tg \, \psi = \frac{r\dot{\varphi}}{\dot{r}}$$

or after substituting Equation (2-3) and (2-5):

$$tg \, \psi = \frac{1}{c} \sqrt{\frac{e}{2m}} \cdot \frac{1}{\sqrt{V^* - V}} \cdot \frac{1}{r} \cdot \int_{r^*}^{r} r \, H(r) \, dr \qquad (2\text{-}6)$$

An ion formed at the anode $(r^* = R_1)(V^* = V_1)$ will have the deflection angle $\bar{\psi}$ at the cathode $(r = R_2)(V = 0)$

$$tg \, \bar{\psi} = \frac{1}{c} \sqrt{\frac{e}{2m}} \cdot \frac{1}{\sqrt{V_i}} \cdot \frac{1}{R_2} \cdot \int_{R_1}^{R_2} r \, H(r) \, dr \qquad (2\text{-}7)$$

9

This angle is independent of the specific electric field distribution and depends only on the voltage applied between the electrodes and on the mass and charge of the ions. However, the shape of the magnetic field has a slight influence since a stronger field in the center is less effective than the same field more outside.

Ions which are formed more outside are deflected according to Equation (2-6) which can be written for $r = R_2$ as follows:

$$\operatorname{tg} \psi / \operatorname{tg} \overline{\psi} = \sqrt{\frac{V_1}{V^*(r^*)}} \int_{r^*}^{R_2} r\, H(r)\, dr \Big/ \int_{R_1}^{R_2} r\, H(r)\, dr \qquad (2\text{-}8)$$

This equation describes ψ as a function of the point of ionization r^*. This function will later be calculated numerically for different field combinations. The deflection ψ is independent of the place of ionization r^* if $\dfrac{d\psi}{dr^*} = 0$, which is the condition for velocity focusing. However, it should be mentioned that this kind of velocity focusing is slightly different from the meaning usually attributed to this name because it does not include the effect of the initial velocities.

2.1.2 Magnetic Deflection Outside the Exit Hole.

2.1.2.1 Magnetic FringeField Effect.

The electric field is confined between the electrodes R_1 and R_2 (See Figure 2-1). Outside R_2 the electric field shall be zero and the particle velocity constant.

10

The magnetic field cannot be confined as well as the electric field and a small fringe field will always be present outside R_2. This field will deflect the beam further, and will be more effective for less energetic particles and change the conditions for velocity focusing.

For small angles ψ where $\dot{x} \approx v$ one obtains

$$\frac{dy}{dx} = tg\ \psi + \frac{e}{mvc} \int_0^x H(x)dx \qquad (2\text{-}10)$$

and

$$Y = X\ tg\ \psi + \frac{1}{c}\sqrt{\frac{e}{2m}} \cdot \frac{1}{\sqrt{V^*}} \cdot \int_0^X \int_0^x H(x)dx\ dx \qquad (2\text{-}11)$$

Equation (2-11) can be written as

$$\frac{Y}{X \cdot tg\ \overline{\psi}} = tg\ \psi / tg\ \overline{\psi} + F \cdot \sqrt{\frac{V_1}{V^*}} \qquad (2\text{-}11')$$

where

$$F = \frac{\dfrac{1}{X} \displaystyle\int_0^X \int_0^x H(x)dx\ dx}{\dfrac{1}{R_2} \displaystyle\int_{R_1}^{R_2} r\ H(r)\ dr} \qquad (2\text{-}12)$$

11

The constant F has no dimension and describes the relative effective strength of the magnetic fringe field in relation to the main field. It is a function of the magnetic field only and is independent of the particle parameters e, m and V^*.

Substitution of Equation (2-8) in Equation (2-11') results in:

$$\frac{Y}{X \, tg \, \bar{\psi}} = \sqrt{\frac{V_1}{V^*}} \cdot \left\{ \frac{\int_{r^*}^{R_2} rH(r)dr}{\int_{R_1}^{R_2} rH(r)dr} + F \right\} \qquad (2-11'')$$

The right side of this equation is only a function of the geometry of the fields and may have a maximum for certain values of r^* and V^* which describe the condition of velocity focusing. It should be emphasized that this condition is independent of the mass of the ions which means that velocity focusing is achieved simultaneously for all masses. The particle parameters e, m affect only the angle $\bar{\psi}$.

2.1.3 Special Cases.

A. <u>Homogeneous Magnetic Field</u>. For a homogeneous field H(r) = H_o one obtains:

$$tg \, \bar{\psi} = \frac{1}{c} \cdot \sqrt{\frac{e}{2m}} \cdot \frac{H_o}{\sqrt{V_1}} \cdot \frac{R_2^2 - R_1^2}{2R_2} \qquad (2-7A)$$

12

For a given size R_2 of the cathode $\overline{\psi}$ becomes largest for $R_1 \ll R_2$. For a given distance $R_2 - R_1$ between cathode and anode $\overline{\psi}$ becomes largest for $R_1 \gg R_2 - R_1$ which approaches the plane geometry case discussed later; on the other hand, for $R_1 = 0$ the deflection $\overline{\psi}$ is reduced to one-half of the corresponding value of the plane geometry.

      Example: Mass number 4 (He), $V_1 = 900$ volts $= 3$ e.st.u.

       $H_o = 850$ Gauss $R_2 = 1.5$ cm $R_1 = 0.5$ cm

$$tg\ \overline{\psi} = \frac{850}{3 \times 10^{10}} \sqrt{\frac{4.8 \times 10^{-10}}{2 \times 4 \times 1.6 \times 10^{-24} \times 3}}\ \frac{1.5^2 - 0.5^2}{2 \times 1.5}\ ,$$

$$tg\ \overline{\psi} = \frac{0.85}{\sqrt[3]{8}} \cdot \frac{2}{3} = 0.066; \qquad \overline{\psi} = 3.8^o$$

For a homogeneous field one obtains also:

$$tg\ \psi / tg\ \overline{\psi} = \sqrt{\frac{V_1}{V^*}}\ \cdot\ \frac{R_2^2 - r^{*2}}{R_2^2 - R_1^2} \qquad\qquad (2\text{-}8A)$$

For ions formed at the anode ($V^* = V_1$ and $r^* = R_1$) one obtains $\psi = \overline{\psi}$ as expected and for the cathode ($V^* = 0$ and $R^* = R_2$) the result becomes undefined. However, since for points near the cathode V^* is proportional to $R_2 - r^*$, the nominator approaches zero linearly and the denominator as the square root of the distance to the cathode. Therefore, ψ approaches zero if the ionization takes place near the cathode.

13

Equation (2-8A) shall now be evaluated for the three typical electric fields mentioned above.

Case (a) Spherical condensor:

$$\frac{V^*}{V_1} = \frac{R_2 - r^*}{R_2 - R_1} \cdot \frac{R_1}{r^*} \qquad (2\text{-}9a)$$

Case (b) Cylindrical condensor:

$$\frac{V^*}{V_1} = \frac{\log R_2 - \log r^*}{\log R_2 - \log R_1} \qquad (2\text{-}9b)$$

Case (c) Plane condensor

$$\frac{V^*}{V_1} = \frac{R_2 - r^*}{R_2 - R_1} \qquad (2\text{-}9c)$$

One can easily see that in all three cases $V^* = 0$ for $r^* = R_2$ and $V^* = V_1$ for $r^* = R_1$. Further, if $R_2 - R_1 \ll R_1$ or if R_1, r^* and R_2 are about the same size, Equation (2-9a) and (2-9b) converges into Equation (2-9c).

Figure (2-2) shows the potential distribution for the three cases for a typical field with $R_1 = 0.5$ cm and $R_2 = 1.5$ cm. The actual field in an inversed magnetron gauge is close to Case (b) in the vicinity of the anode R_1 and close to Case (a) in the vicinity of the cathode R_2.

14

The shape of the potential distribution can be modified to some extent by the geometry of the electrodes. The negative space charge increases the slope near the anode and decreases it near the cathode which brings the potential distribution even closer to Case (a).

Figure 2-3 has been obtained by evaluation of Equation (2-8A) for the three cases mentioned above and shows the deflection angle ψ as a function of V_1/V^*. The abscissa in this graph is inverse proportional to the ion energy or proportional to the deflection of the beam in a transverse electrostatic deflecting field. The ordinate is proportional to the magnetic deflection. Therefore, the graph corresponds to the parabolas obtained on the photographic plate of a Thomson's mass spectrograph. One of these parabolas has been plotted for comparison. The main difference between Thomson's spectrograph and the new arrangement is the fact that in Thomson's instrument all particles, regardless of their energy, are passing the same length of the magnetic field whereas in the new setup the slower particles, which have been ionized near the cathode, are passing only a shorter fraction of the magnetic field. Therefore, their magnetic deflection is less than in Thomson's instrument. This effect is most pronounced in the homogeneous Case (c) where the strong electric field is shifted towards the cathode.

The important feature of these curves is the fact that some of them have a maximum. This means that a small variation of the energy V^* does not affect the magnetic deflection. In other words, these

setups provide velocity focusing which is essential for the use of an ion source having such a wide energy spread as for instance the inversed magnetron. In order to make use of the velocity focusing, it is necessary to eliminate ions with those velocities which are largely different from the ones which provide velocity focusing. Higher velocities can be avoided easily by increasing the diameter of the anode and reducing its potential corresponding to a point near the maximum of the curves in Figure 2-3. Lower velocities can be suppressed by a retarding potential on the ion collector. Under these conditions the curve of Figure 2-3 will be reduced to short and essentially straight horizontal lines.

Figure 2-4 shows the effect of the fringe field for the Case (Ab). Increasing fringe fields (larger values of F) shift the maximum to lower energies and widen the maximum. For $F = 0.3$ and $V_1/V^* = 4$ the maximum becomes a point of inflexion which means velocity focussing of second order. In praxis, it will be more advantageous to operate at a smaller value of F, for instance 0.25, which provides fair focusing over a very wide energy range $V_1/V^* = 2.2 - 7$. In this case the focusing error would only be $\pm$ 1% which would limit the resolution to 1: 100. The resolution may be more limited due to the initial velocity of the ions, the electric fringe field near the exit hole and the finite size of the exit hole. Similar curves as shown in Figure 2-4 can be plotted for the Cases (Aa) and (Ac) which will require different values of V_1/V^* as a

16

function of F. The purpose of these calculations is not so much an accurate computation of the system performance but rather a more qualitative description of the effect of the variation of each parameter. A curve as the one shown in Figure 2-4 can be obtained experimentally more easily and accurately for the actual field arrangement. It cannot be expected that initially this experimental curve will be horizontal. However, by increasing or decreasing the magnetic fringe field it should be possible to achieve energy focusing over a wide range.

B. <u>Magnetic Dipole Field</u>. Preliminary measurements with Alnico VIII magnets, 3.6 cm OD and 4.0 cm long, provided a maximum field at the surface of about 1000 Gauss and a field distribution in the equatorial plane according to Equation (2-12).

$$H = A/r^3 \qquad\qquad (2\text{-}12)$$

The field can be pretty well described by the above-mentioned law with the constant $A = 6000$, especially if the shape and size is similar to the one investigated. The constant, A, is roughly proportional to the volume of the magnet.

The integral in Equation (2-5) becomes in this case:

$$\int_{r*}^{r} r\, H\, dr = A \int_{r*}^{r} \frac{dr}{r^2} = A \left(\frac{1}{r*} - \frac{1}{r} \right)$$

17

and therefore Equation (2-7)

$$\operatorname{tg} \bar{\psi} = \frac{1}{c} \sqrt{\frac{e}{2m}} \frac{1}{\sqrt{V_1}} \cdot \frac{A}{R_2} \left(\frac{1}{R_1} - \frac{1}{R_2} \right) . \qquad (2\text{-}7\,B)$$

This expression has a flat maximum for $R_2 = 2 R_1$ which means that for this condition maximum deflection is achieved.

For $R_2 = 2R_1$ one obtains:

$$\operatorname{tg} \bar{\psi} = \frac{1}{4c} \sqrt{\frac{e}{2m}} \frac{1}{\sqrt{V_1}} \cdot \frac{A}{R_1{}^2} . \qquad (2\text{-}7\,B')$$

Since R_1 is proportional to the linear size of the magnet, the factor $A/R_1{}^2$ is also a linear function of the size of the magnet. This means that the deflection ψ and the resolution are proportional to the linear dimensions of the magnet.

Example:

Mass number 4, $V_1 = 900$ V = 3 e.st.u.; A = 6000; $R_1 = 1.8$ cm

$$\operatorname{tg} \bar{\psi} = \frac{1}{4 \times 3 \times 10^{10}} \sqrt{\frac{4.8 \times 10^{-10}}{2 \times 4 \times 1.6 \times 10^{-24} \times 3}} \cdot \frac{6000}{1.8^2} = \frac{1}{12} \sqrt{\frac{1}{8}} \frac{6}{1.8^2} = 0.055$$

$\bar{\psi}$ equals to 3.1° or is about the same size as in the homogeneous case discussed before.

18

Equation (2-8) becomes in this case

$$
\mathrm{tg}\ \psi/\mathrm{tg}\ \bar{\psi} = \sqrt{\frac{V_1}{V^*}\frac{\frac{1}{r^*}-\frac{1}{R_2}}{\frac{1}{R_1}-\frac{1}{R_2}}} = \sqrt{\frac{V_1}{V^*}} \cdot \frac{R_2 - r^*}{R_2 - R_1} \cdot \frac{R_1}{r^*} \ . \qquad (2\text{-}8\text{B})
$$

This equation has been plotted in Figure 2-5 for a spherical electric field (Case Ba) and for a plain electrical field (Case Bc). Comparison between Figure 2-5 and Figure 2-3 reveals that the inhomogeneous magnetic field causes a much more rapid drop of $\mathrm{tg}\ \psi/\mathrm{tg}\ \bar{\psi}$ which simplifies compensation by the magnetic fringe field.

The effect of the magnetic fringe field in Case (Ba) is shown in Figure 2-6. Velocity focusing near the anode ($V_1/V^* = 1$) is obtained for F = 0.7 compared to - 0.2 for Case (Ab) as shown in Figure 2-4. The advantages of the dipole field are that in this case the fringe field may have the same direction as the main field and can be considerably larger resulting in about twice the beam deflection Y.

The actual field does not follow exactly the law of Equation (2-12) and can be modified to some degree by special shaping of the magnet. By this means it should be possible to extend the flat part of the curves in Figure 2-6 over an even larger energy range. The actual shape of these curves too has to be determined experimentally.

2.2 PLANE GEOMETRY

Early experiments have indicated that the geometrical beam spread can be reduced considerably if the cylindrical geometry of the anode is replaced by a plane one. This means that in the middle plane of the discharge chamber the electric lines of force are parallel to the x-axis, at least in the neighborhood of the beam. Figure 2-7 shows the coordinate system x,y with its origin at the exit hole in the cathode. The anode has the abscissa x_1. The electric potential is independent of y and only a function of x. However, because of the rather limited extension normal to the drawing plane of Figure 2-7 it can not be expected that the electrical field strength between anode and cathode is constant; it is stronger at the anode, and weaker at the cathode. The magnetic field is normal to the plane of drawing; it is also independent of y and only a function of x. The electric field is confined to the space between anode and cathode and is zero outside of the cathode for positive values of x. The magnetic field is stronger at the anode and falls off rather rapidly for positive values of x without ever reaching zero exactly.

The computation of the orbits follows closely the method previously described. Here too, only small deflections are considered where $\dot{x} = v$, or

$$\dot{x} = \sqrt{\frac{2e}{m} (V^* - V)} \qquad (2\text{-}3p)$$

20

The force equation in the y direction is given by

$$m \ddot{y} = \frac{e}{c} H \dot{x} \qquad (2\text{-}4p)$$

which can be integrated resulting in

$$\dot{y} = \frac{e}{mc} \int_{x^*}^{x} H \, dx \qquad (2\text{-}5p)$$

x^* (negative) is the abscissa of the point of ionization, where the velocity is assumed to be zero. The deflection ψ of the beam against the x-axis is given by

$$tg \ \psi = \frac{\dot{y}}{\dot{x}}$$

or after substituting Equation (2-3p) and (2-5p)

$$tg \ \psi = \frac{1}{c} \sqrt{\frac{e}{2m}} \ \frac{1}{\sqrt{V^* - V}} \int_{x^*}^{x} H \, dx \qquad (2\text{-}6p)$$

Formula (2-6p) is quite similar to (2-6) with the only exception that in Equation (2-6) the factor r in the integral and $\frac{1}{r}$ in front of it puts more weight to the magnetic field near the cathode.

An ion formed at the anode ($x^* = x_1$, $V^* = V_1$) will have the deflection angle $\bar{\psi}$ at the cathode (x = 0, V = 0)

$$tg \; \overline{\psi} = \frac{1}{c} \sqrt{\frac{e}{2m}} \; \frac{1}{\sqrt{V_1}} \int_{x_1}^{o} H(x) \; dx. \qquad (2\text{-}7p)$$

This angle is again independent of the specific electric field distribution and depends only on the voltage applied between the electrodes and on the mass and charge of the ions. The integral is equal to the product of length of travel x_1 (negative) in a magnetic field of the average strength $\overline{H}$ between $x = x_1$ and 0

$$\overline{H} \; (x_1, 0) = \frac{1}{-x_1} \int_{x_1}^{o} H(x) dx$$

which results in

$$tg \; \overline{\psi} = \frac{1}{c} \sqrt{\frac{e}{2m}} \; \frac{-x_1 \cdot \overline{H}(x_1, 0)}{\sqrt{V_1}} . \qquad (2\text{-}7p')$$

Ions which are formed between anode and cathode at the point $x=x^{*}$ are deflected according Equation (2-6p). For $x = 0$ and $V = 0$ this equation can be written:

$$\frac{tg \; \psi}{tg \; \overline{\psi}} = \sqrt{\frac{V_1}{V^{*}}} \cdot \int_{x^{*}}^{o} H(x) dx \Big/ \int_{x_1}^{o} H(x) dx \qquad (2\text{-}8p)$$

or

$$\frac{tg \; \psi}{tg \; \overline{\psi}} = \sqrt{\frac{V_1}{V^{*}}} \cdot \frac{x^{*} \cdot \overline{H}(x^{*}, 0)}{x_1 \cdot \overline{H}(x_1, 0)} . \qquad (2\text{-}8p')$$

22

If the magnetic field is homogeneous, then $\bar{H}(x^*,0) = \bar{H}(x_1,0) = H$ and Equation (2-8p') becomes:

$$\frac{tg\ \psi}{tg\ \psi} = \sqrt{\frac{V_1}{V^*}} \cdot \frac{x^*}{x_1} \quad . \tag{2-8p''}$$

.Wide range energy focusing can be achieved if ψ is independent of x^* which requires that V^* is proportional to x^{*2}. Such a field can be made between hyperbolic electrodes. However, its value is limited by the fact that the real magnetic field cannot be exactly homogeneous for $X < 0$ and zero for $X > 0$. Nevertheless, it is expected that electrode shapes can be calculated which will provide wide range energy focusing even for the case of a real magnetic field.

The fringe field effect is still described by Equation (2-11) and (2-11'); however, the fringe field constant F has to be calculated from:

$$F = \frac{\frac{1}{X} \int_o^x \int_o^x H(x)dx\ dx}{\int_{x_1}^o H(x)dx} \quad . \tag{2-12p}$$

Example: Test model 1

The real magnetic field H and the average field $\bar{H}$ of the model 1 test system is shown in Figure 2-8.

23

For hydrogen atoms (m = 1.6 x 10^{-24}g, e = 4.8 x 10^{-10} e.st.u.) and for V_1 = 900 volts = 3 e.st.u. and $\overline{H}(x_1,0)$ = 735 Gauss and x_1 = -- 2.2 cm, one obtains from Equation (2-7p')

$$\text{tg } \overline{\psi} = \frac{1}{3 \times 10^{10}} \cdot \sqrt{\frac{4.8 \times 10^{-10}}{2 \times 1.6 \times 10^{-24}}} \cdot \frac{2.2 \times 735}{\sqrt{3}} = \frac{2.2 \times 0.735}{3 \sqrt{2}} = 0.38.$$

The fringe field constant (2-12p) can be calculated graphically using Figure 2-9:

$$F = \frac{613}{2.2 \times 735} = 0.38$$

For the most energetic particles where $V^* = V_1$ and $\psi = \overline{\psi}$, one obtains from Equation (2-11')

$$\frac{Y}{X \text{ tg } \overline{\psi}} = 1 + 0.38 = 1.38$$

In this case the fringe field increases the total deflection by 38%. This fraction can be altered over a wide range by shielding, movement of the magnet or by auxilliary magnets outside the discharge chamber.

For X = 10.25" one obtains a deflection Y = 5.4" for hydrogen atoms. For other masses and voltages the following deflections should be expected:

24

TABLE 2-1

	M	V_1=900 volts	1500 volts	3000 volts
H	1	Y = 5.4"	4.15	2.95
H_2	2	3.8	2.95	2.08
He	4	2.8	2.10	1.48
N	14	1.45	1.12	0.79
H_2O	18	1.27	0.98	0.69
N_2	28	1.02	0.79	0.56
A	40	0.85	0.65	0.46
Hg	200	0.38	0.30	0.21

The electric field of model 1 can only be estimated very roughly and is shown in Figure 2-10. It has been assumed here that the field penetration into the small tube with the exit hole is negligible. The field between anode and cathode is by no means linear because of the very small flat surface of the anode, the curvature of the cathode and the narrow side walls. However, the main unknown of the electric field distribution is the effect of the negative space charge which will further increase the field strength near the anode and reduce the field near the cathode. The deflection of ions formed in the space between anode and cathode has been computed using Equation (2-8p') with the magnetic field distribution of Figure 2-8 and the electric field distribution of Figure 2-10. The results are plotted in Figure 2-11 which shows that lower energy particles are deflected more. Velocity focusing can be achieved by reducing the length of the tube which supports the exit hole or by shielding the magnetic field in this tube.

SECTION 3

DESIGN STUDIES FOR PERMANENT MAGNETS

3.1   FRINGE FIELDS OF DIFFERENT MAGNET DESIGNS

It has been shown in Section 2 that the velocity focusing proper-
ties depend very much on the distribution of the magnetic fringe field.
It was decided to measure the actual field of different magnet designs
to provide a realistic basis for the computations in Section 2.   One
objective of these tests was to find what field strength can be achieved
in a volume of a few cubic inches with a reasonably small magnet.   First,
the dipole fields of cylindrical permanent magnets of widely different
dimensions were measured.   The maximum field at the equator was essen-
tially independent of the size and shape of the magnet and reached, in
general, values between 400 and 600 Gauss; however, freshly charged
Alnico VIII magnets produced fields up to 1000 Gauss.   These experiments
were made with Alnico V and VIII and with Indox V.   The field obtained
with Alnico V was somewhat smaller than with the two other materials
because of the high demagnetization force which is characteristic for
a small magnet with a wide air gap.   The fringe field is about propor-
tional to the -3rd power of the distance from the center of the cylinder.

Longer cylinders, composed of two or more short cylinders, have produced a more extended fringe field, but have not provided a significantly stronger field at the surface.

In order to obtain a stronger field in the gap, it is necessary to shorten the magnetic circuit with a yoke. Since Alnico VIII and Indox V are highly oriented materials, which can be obtained only in very simple shapes, it is necessary to make the yoke out of Armco iron. This increases the weight without increase of the stored magnetic energy. For the Martian mass spectrometer, where minimum weight is of extreme importance, a specially designed magnet, which consists entirely of Alnico V, might be better. No experiments have been made so far in this direction because the final field size has not been sufficiently established yet to justify the rather expensive and time consuming fabrication of a custom-made casted magnet. Therefore, all experiments have been made with magnet assemblies consisting of a yoke and pole pieces of Armco iron and two plates of magnetic material. One example is the magnet of test model 1 which is shown in Figure 3-1. The side walls of the discharge chamber were made of Armco iron in order to reduce the gap width and increase the field strength. Figure 3-2 shows the main field and the fringe field of this setup.

It turned out that this design, where the pole pieces are used as walls of the discharge chamber, does not provide sufficient flexibility for field variations in a test model. Therefore, a larger magnet

27

(See Figure 3-7) is used in test model 2 which consists of a non-magnetic

discharge chamber. This test instrument will be used to establish the

best field and electrode configuration. However, the first design is

lighter and will be preferable for the flight model.

3.2 DESIGN OF MAGNETIC YOKES

3.2.1 Magnets of Rotational Symmetry with Cylindrical Yokes.

Experiments were performed to determine the proper shape, size and wall

thickness of the yokes in order to obtain optimum conditions as far as

field strength and minimum weight are concerned. For this purpose a set

of Indox V ring magnets (2 3/4" diameter, 3/8" thick, with 1 1/8" center

hole) was placed within a steel housing as shown in Figure 3-3. The

magnets (1), an aluminum spacer (2) and the top and bottom plates (3) form

a sandwich which is centered by a brass tube (5), a steel ring (4) together

with the two plates (3) forms the yoke. A hole drilled through the yoke

ring and the aluminum spacer allowed to insert the probe of a magnetometer

(Bell, model 240). The magnet was placed on a stage (6) which could be

moved by a micrometer screw (7) in order to obtain maximum accuracy.

Different yoke rings (4) and discs (3) were provided to change the dimen-

sions R, D and B.

For practical purposes three yoke rings were used which allow for

the combinations mentioned in Table 3-1.

TABLE 3-1

	R	D
Ring I	1.50 inch	0.50 inch
Ring II	2.00	0.25
Ring III	2.25	0.25
Rings I and II	1.50	0.75
Rings I, II and III	1.50	1.00
Rings II and III	2.00	0.50

The results of these measurements are plotted in Figures 3-4 and 3-5. A comparison of the curves shows that the shape of the field is only determined by the dimension R and that changes of the dimension D have little effect. Alteration of the dimension B which was accomplished by adding a second pair of discs (3), also gave practically no changes in the field distribution. This means that the walls of the yoke can be reduced below 1/4" without loss of field strength.

A second series of experiments was performed in the same way except that four and six magnetic discs were used instead of the two in the first series. The results for the same gap are shown in Figure 3-6. The differences in the field distribution for different yoke dimensions are similar to those for 1 pair of magnetic discs therefore only one characteristic curve for each setup is shown. The only difference in the three curves is the absolute value of the field maximum, which has risen from 1250 Gauss for one pair of magnetic discs to 1500 Gauss for two pairs of magnetic discs and to 1800 Gauss for three magnetic discs.

The relatively small increase of the magnetic field if two or three pairs of magnetic discs are used indicates that the Indox V magnets are practically saturated. Therefore, no significant gain in field strength can be obtained by adding more units.

3.2.2 Rectangular Magnets, with Yokes Open on Two Sides. Similar experiments as described in paragraph 3.2.1 were performed with Indox V discs of rectangular shape (3" by 3", 3/8" thick with a 1 1/4" round center hole). The yokes were of the normal box type as shown in Figure 3-7, and consisted of Armco steel plates. The field was measured in two directions as indicated by the sketch on Figure 3-8.

The results are basically the same as the ones obtained with the magnets of rotational symmetry. The thickness of the yoke plates 1/8" resp. 1/4", has practically no influence on the field distribution. The addition of a second pair of magnetic discs raised the maximum value of the field only from 800 to 860 Gauss. The field distribution in the direction towards the yoke and towards the open side are not much different as demonstrated by the two curves in Figure 3-8.

3.3 SHIELD EXPERIMENTS

Extensive experiments were made in order to determine the shield properties of different materials and also the limits of any shielding due to remanent magnetism in the shield material. Because of the complexity of the problem, no accurate calculations can be made, all parameters for a design have to be determined by experiments. One particular

difficulty in performing these experiments results from the extremely small fields in question. In order to make justified extrapolations, measurements in the milligauss region have to be made with good accuracy. Considering that the earth's magnetic field has a value of approximately 600 milligauss, several precautions must be taken. Particularly, the magnetism in the shield material introduced by the earth's magnetic field can camouflage all the readings and cause severe misinterpretation of the results. A second and very important problem is caused by the fact that any magnet in a shield box creates not only a normal dipole field, but also fields of higher multipoles. These high order multipole fields fortunately decay very fast with distance, but give very distinct angular dependences particularly in the direct vicinity of the shield. To avoid errors, special care was taken to assure that the angle under which the probe saw the magnet was always constant. A field component normal to the earth's magnetic field was measured and the magnet was adjusted in such a direction that its main field was parallel to the measured component. The following results were obtained:

(1) Simple magnetic dipole with 'NETIC" shield box (8"x 8"x6", 0.05" wall). In order to get some basic information about the shielding properties of "NETIC" material, the field of a magnetic dipole consisting of 6 Indox V magnetics 2 3/4" diameter and 2 1/4" total length was measured without and with a shield box. The results are plotted in Figure 3-9. Over a range of 5 orders of magnitude the field follows the theoretical decrease with R^{-3}. The field of the shielded magnet follows with practically the same slope in a parallel line and is

31

diminished by a shield factor, "S" of 34.

(2) Complex magnet with "NETIC" shield box. A similar experiment
as mentioned above was carried out with the rectangular magnet described
in paragraph 3.2.2. The field within the gap was of the order of approx-
imately 800 Gauss and the field in the vicinity of the yoke approximately
4 Gauss. The field of the magnet is plotted in Figure 3-10 with and
without shield box (Curves a and b). From this measurement, three
important conclusions can be drawn:

(a) The field of the unshielded magnet decreases more rapidly
than with R^{-3} and cannot be considered to be a dipole field.

(b) The field of the shielded magnet decreases less rapid
than the field of the unshielded magnet, therefore, the shield factor
depends on the field strength.

(c) The shield factor is much less than in the previously-
described experiment (1) and decreases from 17 to only 4 at the end of
the range. Figure 3-10 indicates that at very low fields the shield
factor seems to approach unity, i.e., that no shielding at all can be
accomplished at very low field intensities. In these cases the external
field is practically determined by the magnetism of the box. A careful
examination of the shield box alone showed several singularities at the
wall with field values up to a few hundred milligauss. Several attempts
to "degauss" the box in a strong AC field were made. Most of the singu-
larities could be eliminated but on the corners of the box, some
singularities remained.

3.4 EXPERIMENTS WITH NETIC AND CONETIC FOILS

The results of the experiments with the shield box indicated that,
because of singularities in the shield box, the effective shield factor
became extremely low at low fields. The small flux density in the shield
itself seems also to diminish the shield factor. Therefore, a new and
last series of experiments were carried out to achieve improved shield-
ing under controlled conditions. Because the magnetic characteristic
of NETIC material shows a relatively poor B-H dependence at very low
fields, CONETIC foil was also used for shielding purposes, which promises
a much better B-H characteristic for low fields. On the other hand,
CONETIC foil becomes saturated at relatively small H values and has to
be shielded from the original magnet by use of NETIC material. The
whole magnet was placed within a wooden box which provided 0.5" spacing
between the magnet and the shield. NETIC foil 0.005" thick was carefully
wrapped around the wooden box in a single layer with a slight overlap.

Finally, the whole unit was shielded with a CONETIC foil 0.005" thick
spaced approximately 1/8" from the NETIC shield. The results are given
in Figure 3-8. Curves c, and c_2 are measured with the magnet in the
same basic position except turned around by 180°; curve c_3 represents
the mean value of both measurements. The residual field has dropped
considerably to approximately 1 milligauss at a distance of R = 20 cm.
Two significant observations can be made:

33

(1) The slope of the curves corresponds to that of the unshielded magnet. Therefore, the shield factor seems to be independent of the field strength.

(2) The value of the shield factor has increased to approximately 60 and is changing only slightly.

It is important to mention that the orientation of the magnet has some influence on the remaining fringe field: the field in the direction of the "open" side of the magnet (curve c_4) is about twice as strong as in a direction perpendicular to it (curves c_1 and c_2). The differences in the slope are insignificant, because of the relatively large measuring error in this low field region. Some small singularities have also been observed, but they affect the field only at distances less than 10 cm from the shield.

The overall shield factor, "S", for this magnet and for this combination of shield materials is plotted in Figure 3-11.

It is very significant to note that the shield factor "S" has a high value of 200 at 1.0 Gauss and still approximately 60 at 0.010 Gauss. The extrapolated curves indicate that it should be possible to reduce the remaining fringe field down to about 1 gamma at a distance of 3 1/2' = 107 cm from the magnet center.

SECTION 4

TEST SYSTEM MODEL 1

The objective of this instrument was to prove the basic feasibility

of the new mass spectrometer and to analyze the ion beam generated by

an inverted magnetron gauge in regard to the mass and energy of the ions.

The location of the ion beam is detected by a collector movable in a

plane normal to the beam. An electric deflection field is used to pro-

duce an energy spectrum of the ions.

Figure 4-1 shows a schematic cross section of the instrument in

plain size. The inverted magnetron gauge consists of an aluminum

housing (1) which contains the grounded cathode ring (2) made of brass

and the aluminum anode (3) which is insulated by the cable end seal (4).

The two sideplates (5) of the discharge chamber are made of Armco iron

and sealed with Viton O-rings. These plates are the polepieces of the

magnet which is shown in Figure 3-1. A short tube (6) is screwed into

the cathode (2) and closed at the upper end by a gold foil (7) which

contains the exit hole for the ion beam. Since this hole is by far too

small to evacuate the upper part of the system, a bypass channel (8) has

been provided for this purpose. This channel acts also as a baffle

which prevents ions from the discharge to diffuse through the pumping channel to the collector. The whole system is evacuated through tube (9). The sample gas is introduced directly into the discharge chamber through the thin tube (10). The ion beam passes through the flexible bellow (11), the electric deflection field (12), the collector diaphragm opening (13) into the ion collector (14). The washers (15) and (16) have been installed to prevent grazing incident reflections of the beam on the walls of the chamber (12) and the tube (17). The discharge chamber (1) is mounted rigidly on the pumping station. The upper part of the system can be tilted around the axes (18) and (19). The locations of these axes are a compromise between the desired position and the limited flexibility of the bellow. The movement is accomplished by two micrometer screws (20) and (21). The screw (20) is motor-driven and used to scan the mass spectrum. The screw (21) is adjusted by hand to measure the electric deflection of the beam in the condensor (12).

The ion current has been measured either by a linear electrometer (Keithley Model 600) or by a logarithmic electrometer (Keithley Model 412) and recorded by a Sanborn recorder model 150-2900 V. At every tenth of an inch of the micrometer position a manual mark was made on the recording. This permitted correlation of the peaks to the position of the collector.

36

TABLE 4-1

BASIC DIMENSIONS OF TEST MODEL 1

Distance anode - cathode	1.4 cm
Distance anode - exit hole	2.2 cm
Distance exit hole - collector hole	17.6 cm
Diameter of cathode	3.1 cm
Diameter of exit hole	0.27 mm
Diameter of collector hole	0.83 mm

Each mark on the recordings correspond to 0.1" micrometer movement or to 2.4 mm collector hole movement.

Average magnetic field between anode and exit hole $\overline{H}(x_1,0)$ = 735 Gauss.

Distance between polepieces = height of cathode cylinder = 1.9 cm.

Diameter of the polepieces 4.0 cm.

SECTION 5

RESULTS OBTAINED WITH TEST MODEL 1

The first measurements were made with a round anode of 1/2" diameter.
The discharge started easily below 1000 volts and causes first effec-
tive outgassing of the electrodes. After a few hours of operation, an
equilibrium is reached between outgassing and absorption and the dis-
charge burns sufficiently stable. Figure 5-1 shows a typical current-
voltage characteristic. The background pressure (in this case,
3×10^{-5} torr) depends slightly on the voltage; it is a minimum around
1000 volts where ion pumping is most effective and is above average at
the top voltage where outgassing is predominant.

Early experiments have indicated that the spread of the beam is
rather wide and it has been expected that a flat geometry of the anode
would reduce the divergence. Experiments with a flat anode (1" x 1/2"
and 1/4" thick) have demonstrated that this is a step in the right di-
rection. However, the discharge was very hard to start and required,
if operated with helium, about 5 kV and a pressure corresponding to
5×10^{-4} torr ionization gauge reading. Below 2×10^{-4} torr the dis-
charge stopped.

Therefore, a compromise was made between these two cases by cutting away almost one-half of the original anode cylinder. This geometry proved to be very useful; the discharge was easy to start and the beam spread significantly reduced. All later-described measurements with Model 1 were made with this anode.

The measurements have been made by moving the collector with constant speed in the direction of magnetic deflection and by simultaneously recording the collector current. The positions of the collector have been marked manually on the recordings. The spectra which have been obtained initially showed a number of peaks which could not be correlated to the gases in the discharge. It has been found that they were caused by reflections of the beam on the walls and could be eliminated by inserting the two diaphragms (15) and (16) shown in Figure 4-1.

The work was first concentrated to identify the background peaks and to establish the mass scale. For this purpose, the following gases have been admitted to the discharge: hydrogen, helium, water vapor, nitrogen, argon and mercury. Figure 5-2 shows typical mass spectra obtained in this way. The background showed three peaks which could be identified as N_2, H_2O and a very small amount of H_2. During these measurements it has been observed that the positions of the peaks depend on the pressure of the gas; this is shown in Figure 5-3. This effect has not been expected; it is probably caused by the space charge of the electron cloud which seems to have an influence on ion orbits which cannot be neglected. The peak shift has been studied extensively

39

as a function of the composition of the admitted gas, the pressure and the particular peak. The effect appears to be the largest for the hydrogen peak at mass 2, especially if helium is introduced into the discharge. In this case, a peak shift of 10% has been observed if the pressure is increased corresponding to an ionization gauge reading from 5×10^{-7} to 1×10^{-5} torr. If mercury vapor is introduced, the shift of the hydrogen peak is much less, which is partially the result of the higher sensitivity of the ionization gauge for mercury vapor. The peaks of higher masses show less shift, but the ratio between shift and deflection is about constant. Figure 5-4 shows the position of different peaks obtained with the same ionization gauge reading 3×10^{-6} torr. The lengths of the horizontal lines corresponds to the peak shift if different gases are introduced. Despite the uncertainty caused by the pressure effect, it can be seen from Figure 5-4 that the mass scale follows well the theoretical law $M^{-1/2}$. However, comparison with Table 2-1 shows that the experimentally observed deflections are smaller than the computed ones. This becomes even more obvious if one investigates the position of the peaks as a function of the discharge voltage. Theoretically, one should expect that Y is proportional to $V^{-1/2}$; however, Figure 5-5 shows large deviations of the observations. (The straight lines are computed; the points represent the observations.) It must be concluded that the potential applied to the anode does not determine completely the field between anode and cathode. The space charge from the trapped electron cloud and from the slow moving ions seems to have a significant influence on the effective total electric field.

The construction of the exit hole diaphragm and its supporting structure has also a large influence on the performance of the instrument. It has already been shown in Section 2 that the distance of the exit hole from the cathode can be used to adjust the velocity focusing conditions. In addition to this, the exit hole acts as a dispersing lens with a focal length proportional to the hole diameter. This lens widens the beam and reduces the resoltuion. This undesirable effect can be reduced by mounting the diaphragm with the exit hole on a short tube which sufficiently shields the hole from the electric field. The lens effect of the hole may be neglected in this case and is replaced by the much weaker lens effect of the tube. However, the electric field in the tube has a component normal to the beam and reduces the dispersion. It is expected that advanced design of the exit hole region may improve significantly the performance of the instrument.

One of the main objectives of the tests with Model 1 was an experimental verification of the velocity focusing properties which were first predicted only theoretically. For this purpose, the beam passed an electrostatic field which deflects the beam in a direction normal to the magnetic deflection. The electric deflection is inversely proportional to the energy of the ions. Figure 5-6 shows the results obtained in this way. Within the very wide energy range from full to half energy, the magnetic deflection is practically constant $Y = 1.44 \pm 0.02$. The energy focusing is adequate to achieve the required resolution. At present, the resolution is limited to much lower values because of the divergence of the beam.

Another important feature of an analytical mass spectrometer is
the relation between peak height and partial pressure. This has been
checked with the argon peak when argon was admitted to the discharge.
The abscissa in Figure 5-7 is the total pressure as read with an
ionization gauge. The argon partial pressure is somewhat lower, especially
near the background pressure. The stars and circles represent two
different runs which coincide fairly well. Above 10^{-5} torr, the peak
height is proportional to the pressure. The deviations below 10^{-5} torr
are partially caused by the background gas which contains only a small
fraction of argon.

During these measurements, a "memory" effect has been observed.
Gas which has been previously analyzed is kept absorped in the elec-
trodes and released more rapidly when a new sample is introduced. This
effect is well known and to some degree common to all mass spectrometers
and ionization gauges. However, it is more pronounced in the new instru-
ment because of the higher voltages and currents in the discharge.
The memory effect hardly affects the analysis of major constituents;
however, some precautions are necessary if minor constituents shall be
analyzed. In this case, the instrument shall either never be exposed
to these gases or shall be well outgassed by operating the discharge
at a pressure of about 5×10^{-5} torr with a heavy gas such as xenon or
mercury vapor. Further tests are necessary to study the effectiveness
of this clean-up procedure.

SECTION 6

TEST SYSTEM MODEL 2

During the work with model 1, several modifications became desirable.

(1) In order to be able to study the effect of shifting the magnet, it was necessary to avoid pole pieces which are a part of the discharge chamber.

(2) A somewhat larger discharge chamber was desirable to permit reduction of the operating voltage.

(3) The shape of the anode and the cathode had to be modified to achieve a more plane geometry near the exit hole.

(4) The housing of the beam section should be wider and shaped in such a way that particles reflected on the walls cannot reach the collector.

(5) The distance between exit hole and collector should be substantially reduced to make the basic geometry of the test model more similar to the anticipated flight version. However, the detailed design is quite different and more complex in order to permit investigation of the energy distribution.

(6) The housing of the beam section shall be insulated and kept on a negative potential in order to be able to retard the ions in front of the grounded collector diaphragm and to suppress low energy ions which may spoil the resolution.

(7) The collector has to be well shielded to prevent any leakage current or noise from the housing kept under high voltage.

Figure 6-1 shows a schematic cross section of the basic system, Figure 6-2 a photograph of it, and Figure 6-3 an over-all picture of the whole test setup. Referring to Figure 6-1, one sees the ionization chamber housing (1), which acts as the cathode, and a square plate (2) in the center which acts as the anode. The exit diaphragm (3) is mounted on a tubular insert (4) which can be adjusted up and down. The diaphragm was originally made of gold foil with a 10 mil hole in the center. This foil sputtered considerably and caused a gold deposit on the anode. The foil has been replaced by an aluminum foil with a 2 mil hole in the center.

The sample gas is introduced directly into the discharge chamber in a similar manner as in model 1. However, the evacuation is done separately from the discharge chamber and the beam chamber in order to further reduce the background pressure.

The beam analyzer section has been completely redesigned. The shorter distance between the exit hole and the collimator hole, with the electric deflection field in between, did not permit a setup as in model 1. In this case it was necessary to move the bellow (5) upward, far beyond the collector. A set of four screws (6) prevent the bellow from collapsing under vacuum. The two micrometer screws (7) and (8) pivot the collector assembly around the points (9) and (10), thus moving the collector hole in the opposite direction. The collector (11) is surrounded by a shield (12) which is insulated from the housing (13). This permits the shield to be kept at ground potential if the housing is charged up to a negative retarding potential. A pair of deflection plates (14) are inserted in the space between exit and collector holes to analyze the energy distribution of the beam.

The scanning of the mass spectrum and the recording is done in the same manner as in model 1. However, the marks on the recording corresponding to certain micrometer positions are now performed automatically.

Table 6-1 shows the basic dimensions of model 2.

TABLE 6-1

Distance anode - cathode	1.3 cm
Distance anode - exit hole	2.2 cm
Distance exit hole - collector hole	8.0 cm
Diameter of exit hole	0.05 mm
Diameter of collector hole	0.50 mm

Each mark on the recordings correspond to 0.025" micrometer movement or to 0.7 mm collector movement. Average magnetic field between anode and exit hole: $\bar{H} (x_1, 0) = 604$ Gauss. Distance between pole pieces: 3.5 cm. Size of pole pieces: 3" x 3" or 7.6 x 7.6 cm.

SECTION 7

TEST RESULTS WITH THE SECOND MODEL

This test system has been in operation for a few weeks only and
the measurements are not completed yet. However, valuable results have
already been obtained. The most important one is the fact that the new
geometry of the discharge chamber reduces substantially the space
charge effects observed with the first model. The shift of the mass
scale as a function of pressure has been practically eliminated. This
will permit use of collectors in fixed positions, permanently tuned for
certain constituents. In addition to this, the peak shift as a function
of discharge voltage follows the theoretical curve much closer than in
model 1.

A modified shape of the anode (see dotted line in Figure 6-1) has
been tested. The purpose of this eccentric shape is to concentrate the
strongest electric field near the exit hole and to produce more ions
just in that region. This should result in a larger ratio of beam
current to discharge current which has been actually observed. However,
the resolution was much reduced and therefore the old square anode

installed again. This experiment showed that the shape of the anode

has a significant effect on the resolution. It is expected that a

concave surface of the anode will yield higher resolution than a flat

surface.

An attempt was made to improve the resolution by reduction of the

size of the exit hole from 10 mil to 2 mil. The achieved improvement

was only one half of the one expected which indicated that the beam

spread is now caused mainly by other factors. The most important one

is the effect of the initial ion energy due to the thermal velocity of

the gas molecules. It might be possible to reduce this effect by

cooling of the discharge chamber.

It has been observed that there are two different stable operating

conditions of the discharge: a low current (smaller than about 30

microamps) and a high current (above 100 microamps) version. The region

between is unstable. The mass spectra of the low current discharge

are in agreement with the expectations. The mass spectra of the high

current discharge are more complicated; some peaks are widened and

even split into doublets, and their position does not fit into the

normal mass scale. It seems that either plasma oscillations or other

secondary effects are responsible for the disturbed behavior. The new

mass spectrometer is a good device to study the phenomena of the cold

cathode discharge and will lead to a better understanding of these

types of vacuum gauges.

SECTION 8

SUMMARY OF THE WORK PERFORMED ON THIS STUDY
CONTRACT AND OF THE RESULTS OBTAINED

The new mass spectrometer principle, which has been studied especially for testing the Martian atmosphere, differs from regular mass spectrometers by the following points:

(1) No hot filament required.

(2) High ionization efficiency due to a magnetically trapped electron cloud.

(3) Very low power consumption of the mass spectrometer ion source, less than 0.1 watt.

(4) No beam collimator between ion source and analyser is required.

(5) The ion source itself acts as the mass analyzer which results in a very compact and simple instrument.

(6) The ion source acts also as its own pump.

The instrument is based on recently discovered velocity focusing properties of a particlar combination of an inhomogeneous electric and magnetic field. The detailed mathematical explanation of this focusing effect is given in Section 2.

A test system has been built in order to verify the theoretical results and to determine the actual performance. This test system is more complicated than the final instrument in order to measure not only the mass but also the velocity distribution of the ions. For this purpose, crossed electric and magnetic deflections have been used in a similar way as in the classical Thomson parabola spectrograph. However, the ions were detected electrically with a Faraday collector movable in two directions. The ion current has been recorded as a function of the magnetic deflection. The flight model would have no electric deflection field but a number of fixed collectors adjusted for expected masses or mass intervals.

Initial experiments showed the occurrence of wall reflections. A substantial improvement has been achieved by inserting of two diaphragms. A number of different mass spectra, obtained after this modification, are shown in Figure 5-2. The resolution which has been obtained so far is adequate to resolve hydrogen, helium, and other light masses but is too small to resolve nitrogen and oxygen. However, some improvements of the resolution are still feasible by modification of the shape of anode and cathode which will result in a narrower beam by increasing the magnetic field and by cooling of the discharge chamber.

The work has been concentrated first to establish a mass scale by introducing successively hydrogen, helium, water vapor, nitrogen, argon, and mercury vapor. The positions of the mass peaks do not agree well

with the computations which were made under the simplifying assumption
of neglecting the space charge. However, the space charge of the
ionizing electron cloud has a determinant effect on the **electric field
distribution**. The density and location of this space charge depends on
the total gas pressure and on the gas composition. As a result of this,
a slight shift of the peaks has been observed if the pressure in the
discharge is increased.

Preliminary experiments with the second test system have
demonstrated one important imporvement: The pressure dependence of the
mass scale has been reduced below the detection limit and is no longer
a drawback of this instrument.   Also, the resolution has been
doubled by use of a much smaller exit hole but is still not enough to
separate the nitrogen and oxygen peaks. However it has been found that
the resolution is strongly affected by the shape of the anode. It is
expected that some further improvements of the resolution are possible
by modifications of the geometry of anode and cathode.

Another phenomenon which has been observed is the so-called
"Memory Effect" which means that previously tested samples produce a
background in later experiments. This effect is well known and to some
small extent present in all mass spectrometers. However, in the new
instrument, the memory effect is more pronounced because of the high
discharge voltage and current. The discharge acts as an ion pump:

During prolonged operation an equilibrium between absorption and desorption will be established. After the discharge conditions have been changed, either by increase of the voltage or the pressure, the equilibrium is disturbed and previously pumped gas is released. This means that introduction of a new sample produces not only the peaks specific for this sample but increases also the background left over from previously analyzed samples. It is expected that this effect can be reduced by other cathode materials and by limitation of the operating pressure. Complete elimination of the memory effect is probably impossible and means have to be found to live with it. One way which seems to be feasible is to operate the mass spectrometer between the samples with a gas of high mass, Xe or Hg, which is not expected to be in the samples. The contamination of the instrument with these gases would not be harmful since these mass peaks are far away from the interesting peaks produced by the sample. The bombardment of the electrodes with these heavy ions will outgas and clean the electrodes and substantially reduce the background from previous samples. This effect has been actually observed by operating the tube with mercury.

So far, the performance of the test instruments did not come near the requirements for the Martian probe. On the other side, it must be considered that the mass spectrometer utilizes many new principles and will therefore require a longer time for proper development as than instruments which are based on designs known for decades. It is expected

that considerable improvements can be made in the near future; but at present, it is still impossible to predict to what degree the disturbances can be eliminated and what resolution and accuracy will be actually achieved.

CONCLUSIONS

The experiments have proven that simple mass spectra can be obtained with the new instrument. However, the resolution is far below the requirements for the Martian probe. For this reason, it seems to be premature to start construction of the breadboard model at this time. Nevertheless, the instrument has important good features: very low power consumption and extreme simplicity; only one voltage is required to operate the ion source and no vulnerable filament is necessary. The instrument will be useful for applications where a low resolution is adequate.

ACKNOWLEDGMENTS

LTS18-1810P

Figure 2-1. Coodinate system for axial symmetry.

54
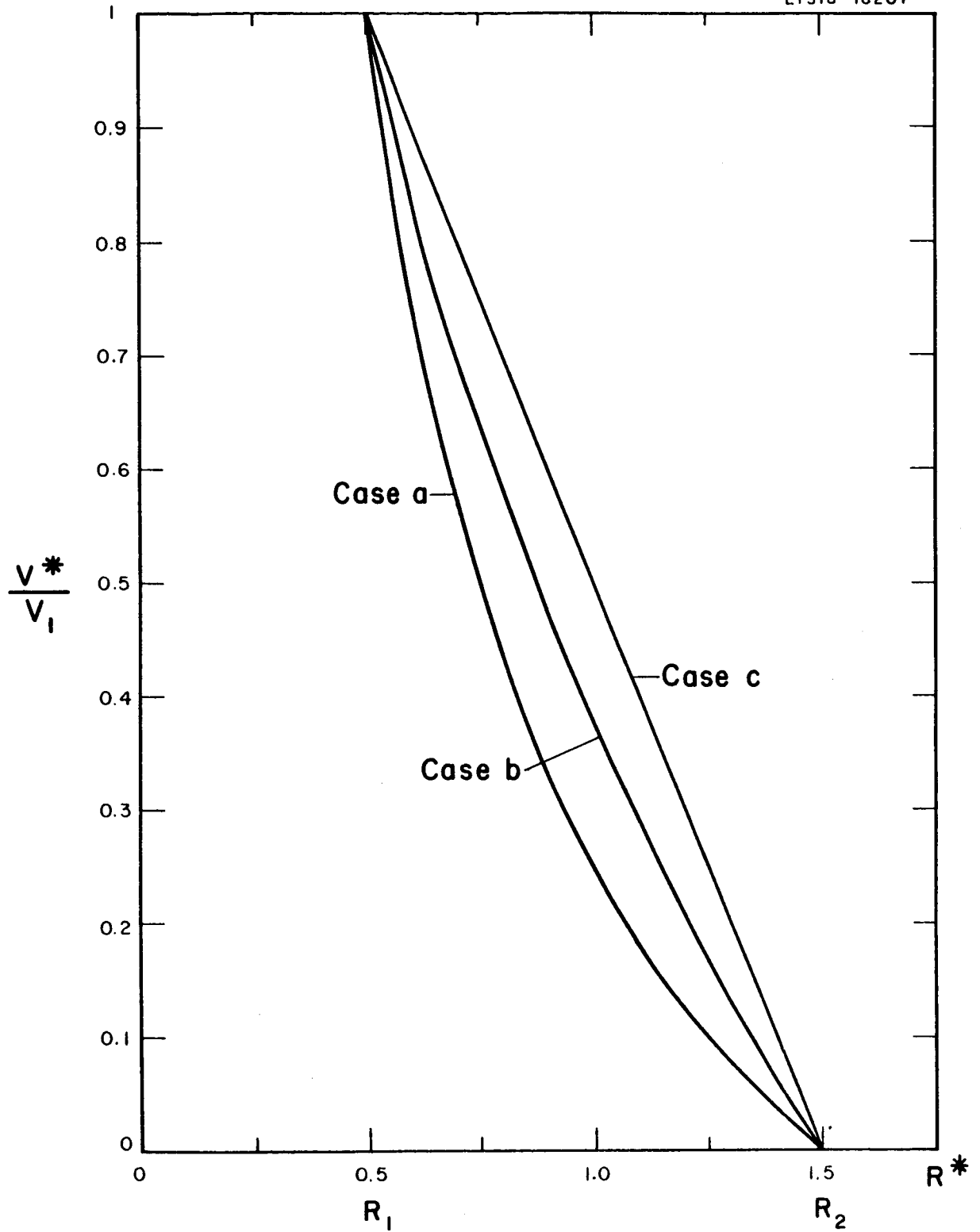
Figure 2-2. Electric field distribution.

Case a: Spherical condensor
Case b: Cylindrical condensor
Case c: Plane condensor

LTS18 - 1830P
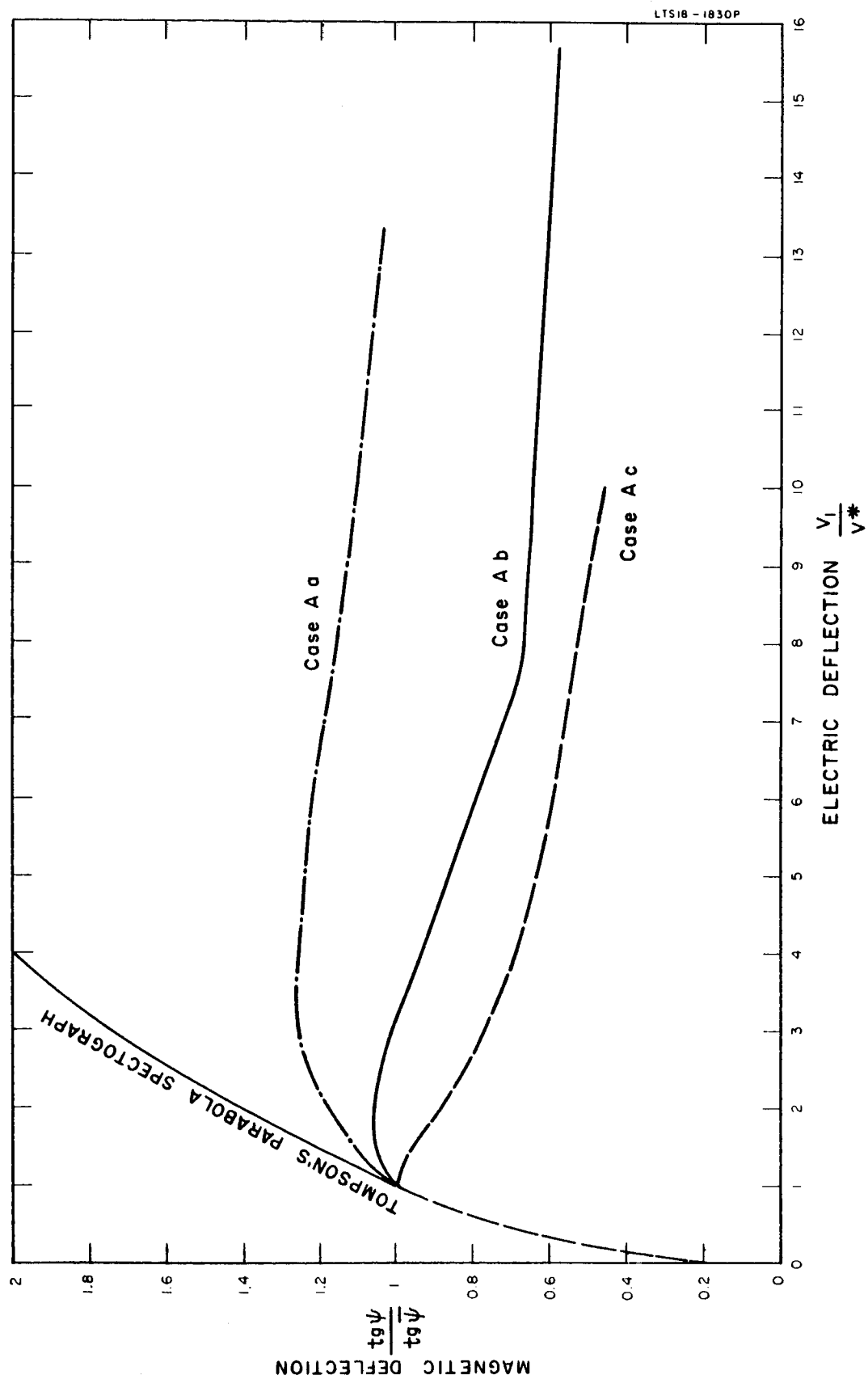
Figure 2-3. Energy dependence of the magnetic deflection (homogeneous magnetic field).
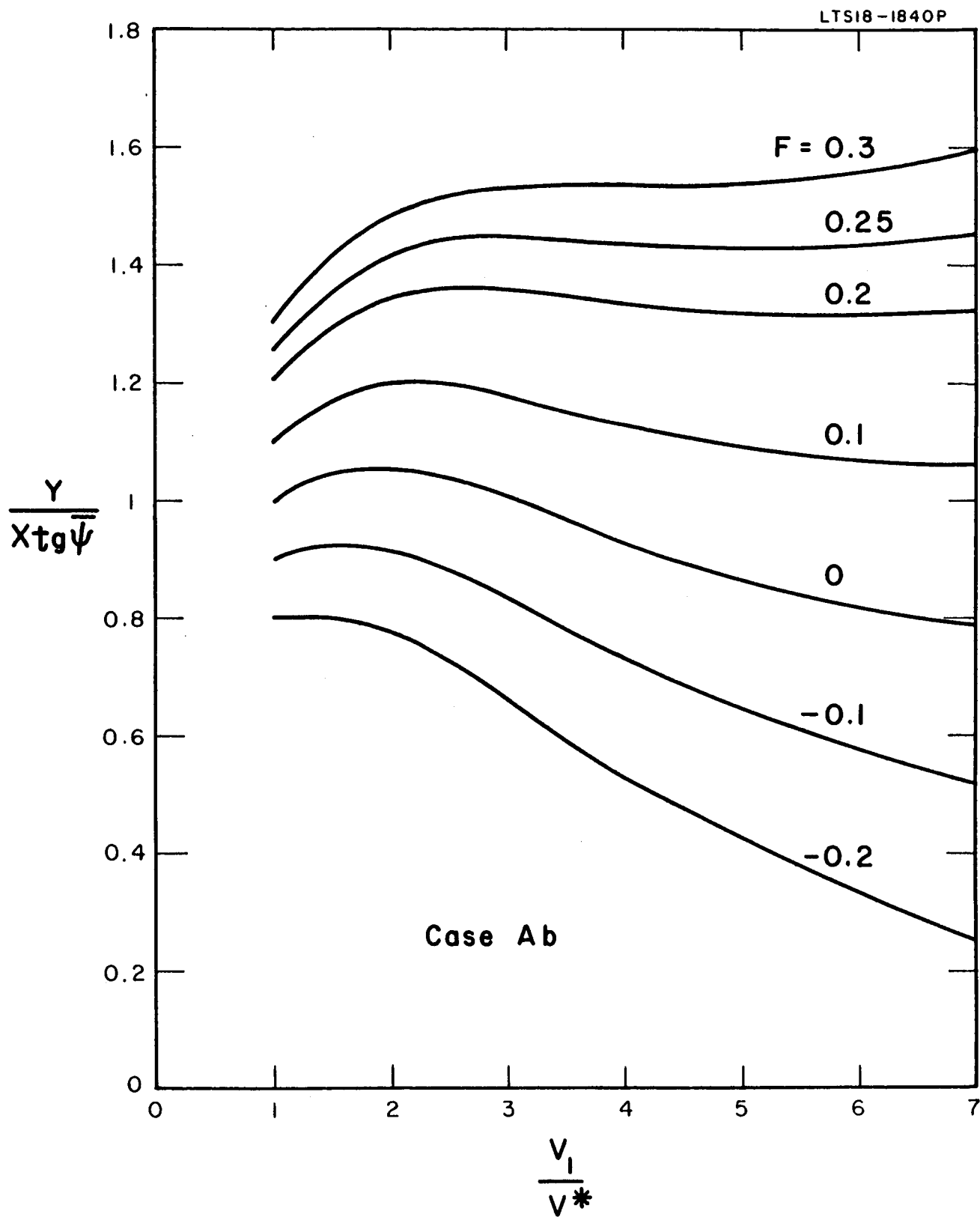
Figure 2-4. Fringe field effect (homogeneous magnetic field).
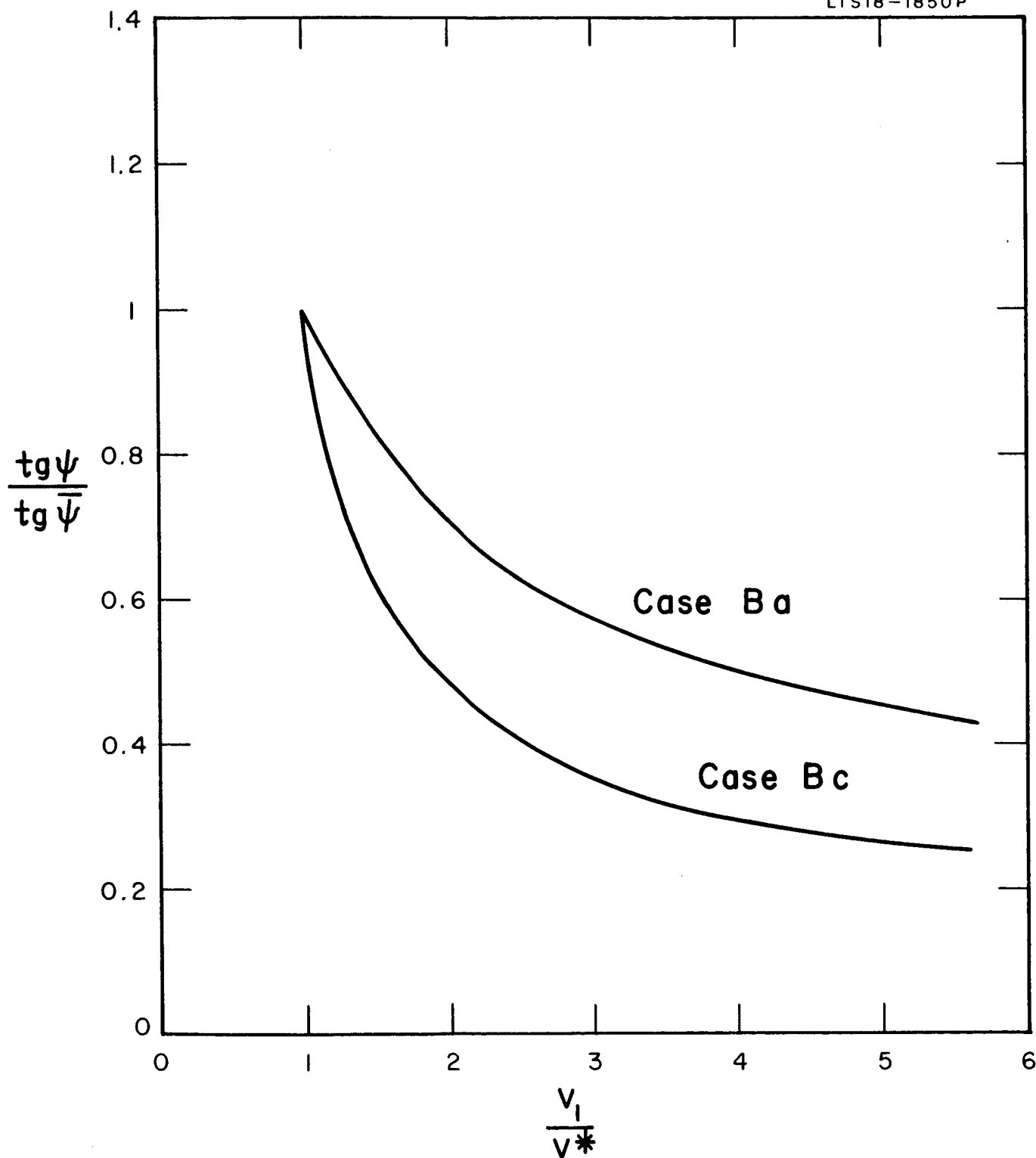
Figure 2-5. Energy dependence of the magnetic deflection
(magnetic dipole field).

58
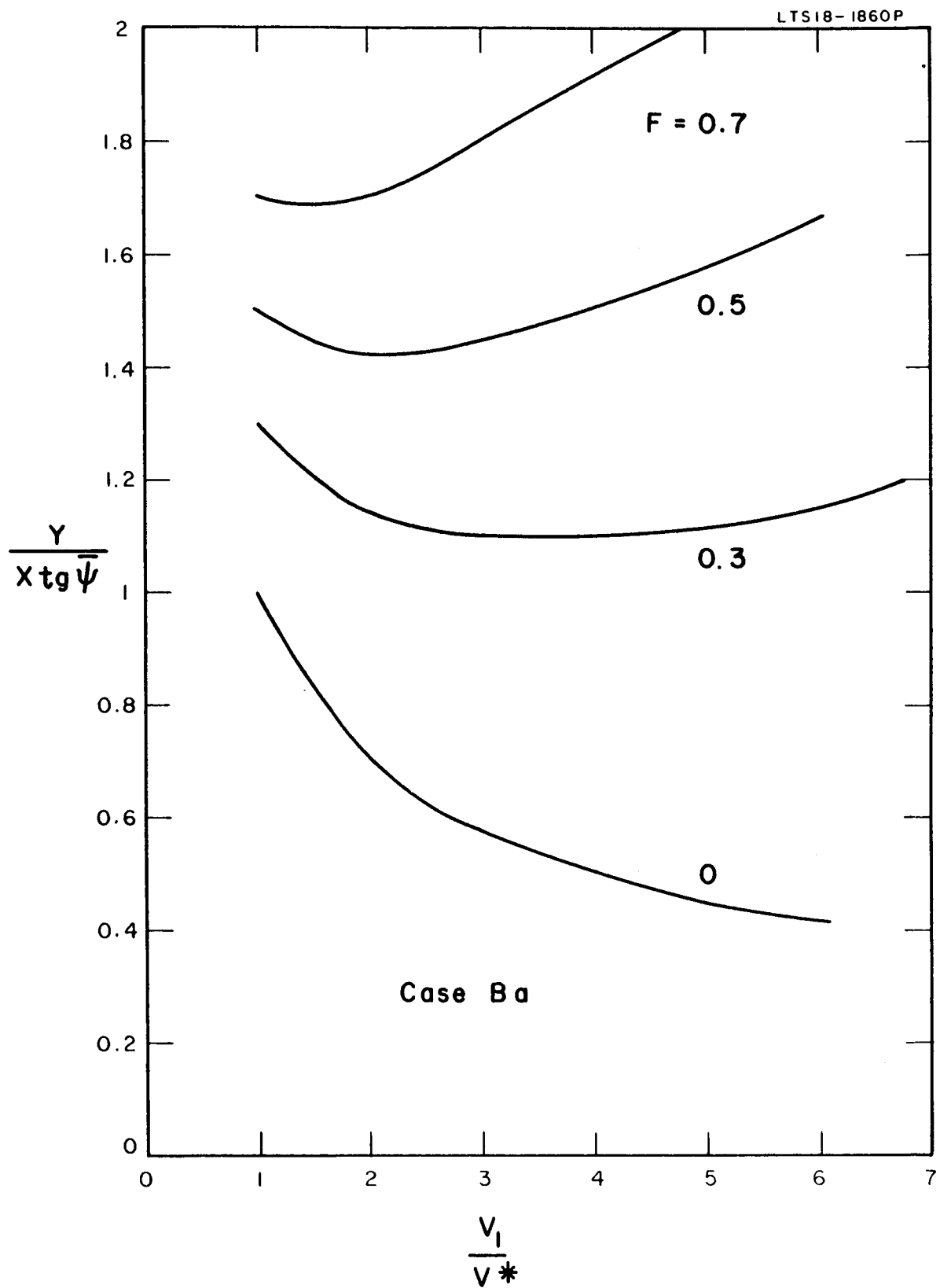
Figure 2-6. Fringe field effect (magnetic dipole field).
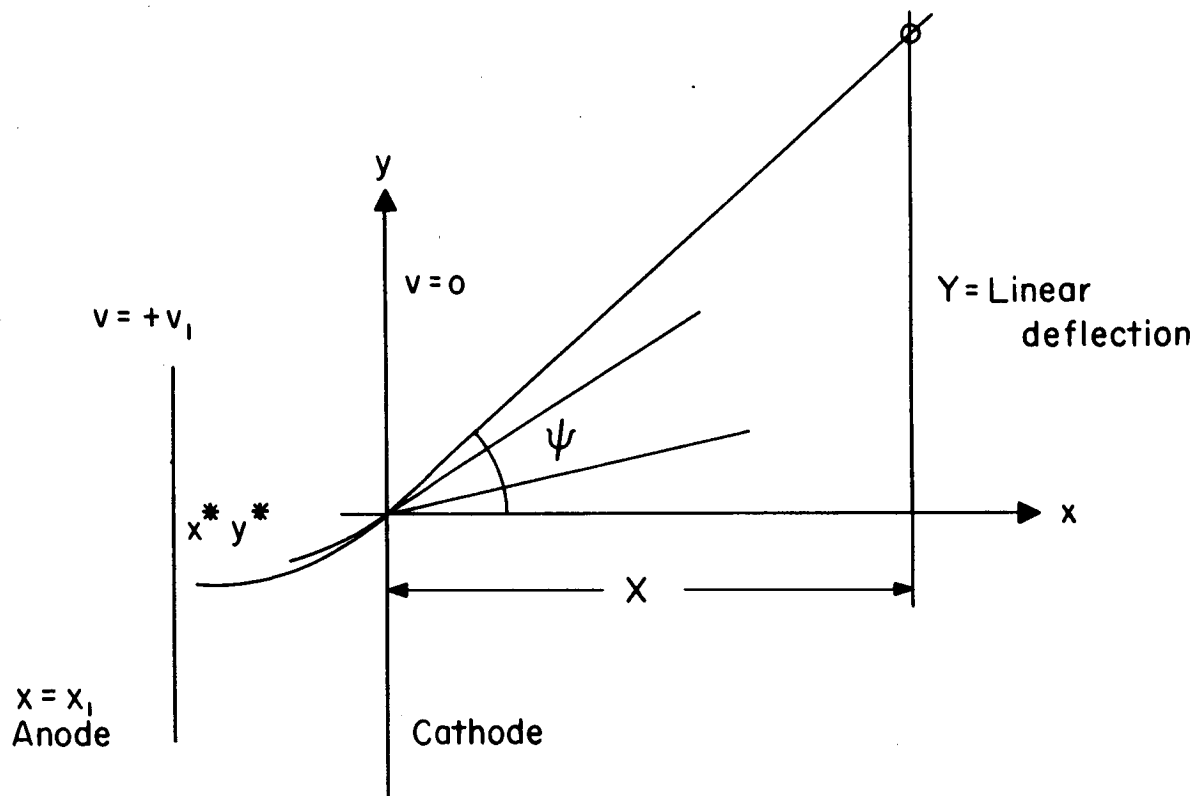
Figure 2-7.   Coordinate system for plane geometry.
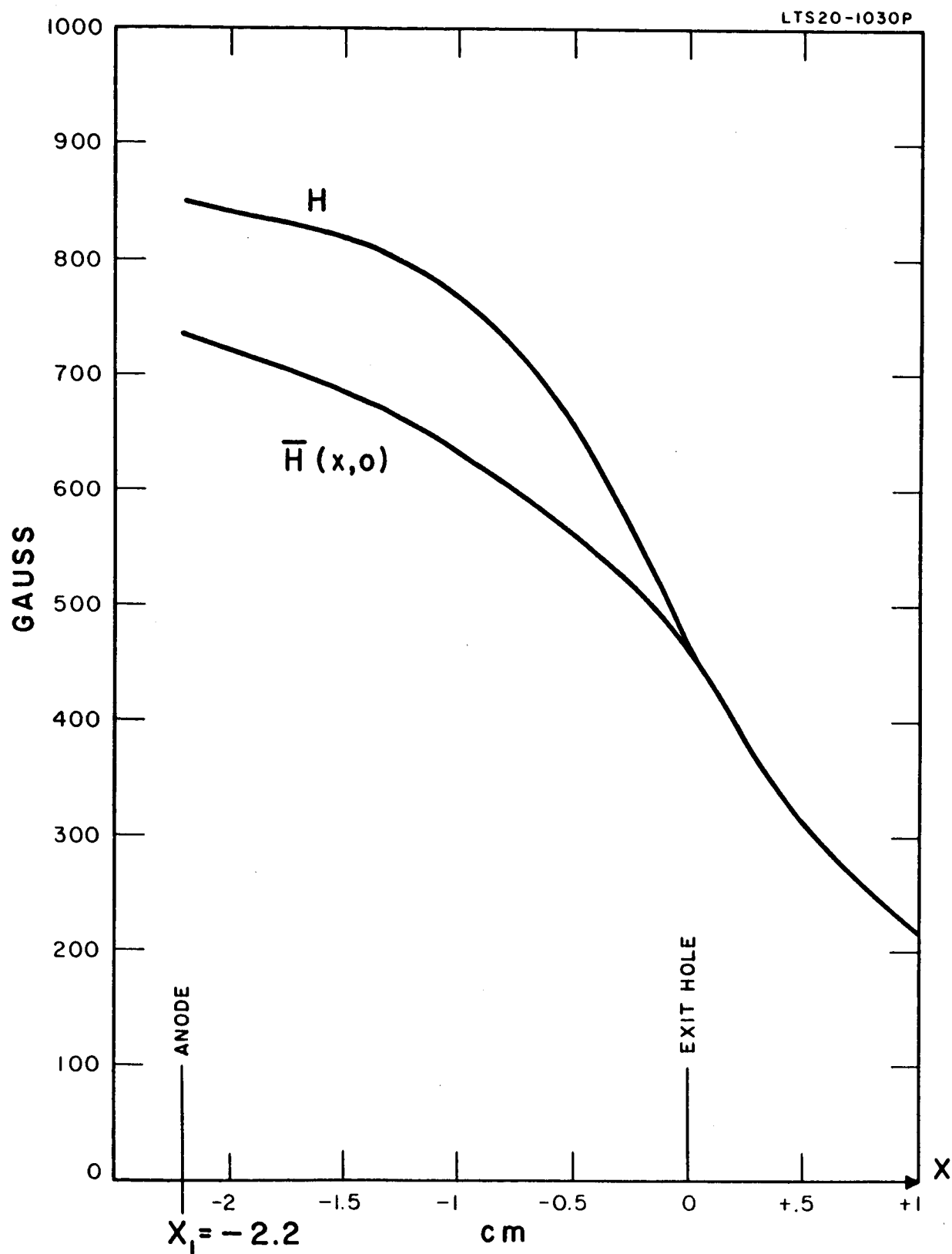
Figure 2-8.   Magnetic field distribution of Test Model 1

H = magnetic field

$\overline{H}(x\ o)$ = average magnetic field between x and o.
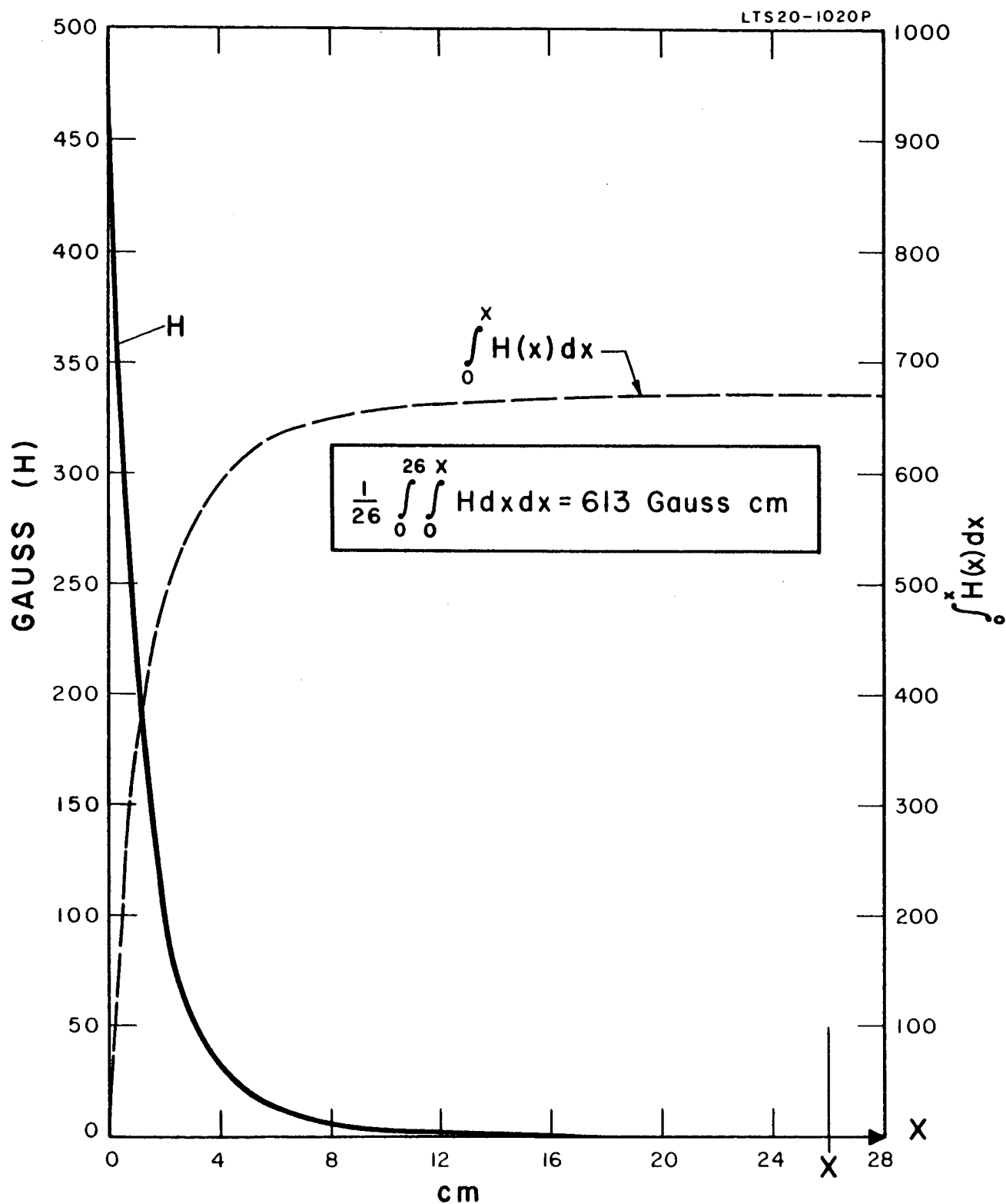
Figure 2-9. Graphic computation of the fringe field integral for
Test Model 1.
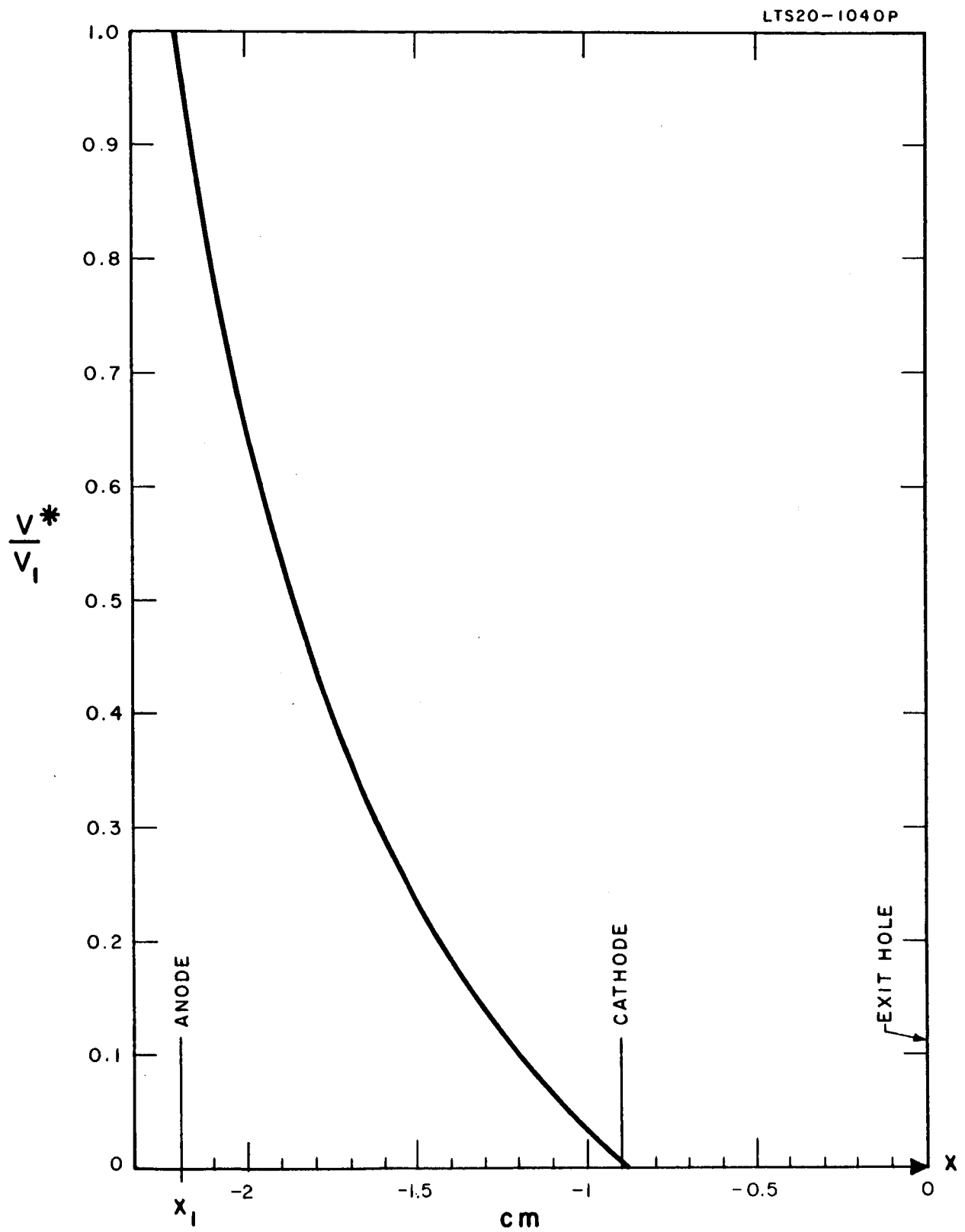
Figure 2-10.   Assumed electric field in Test Model 1.
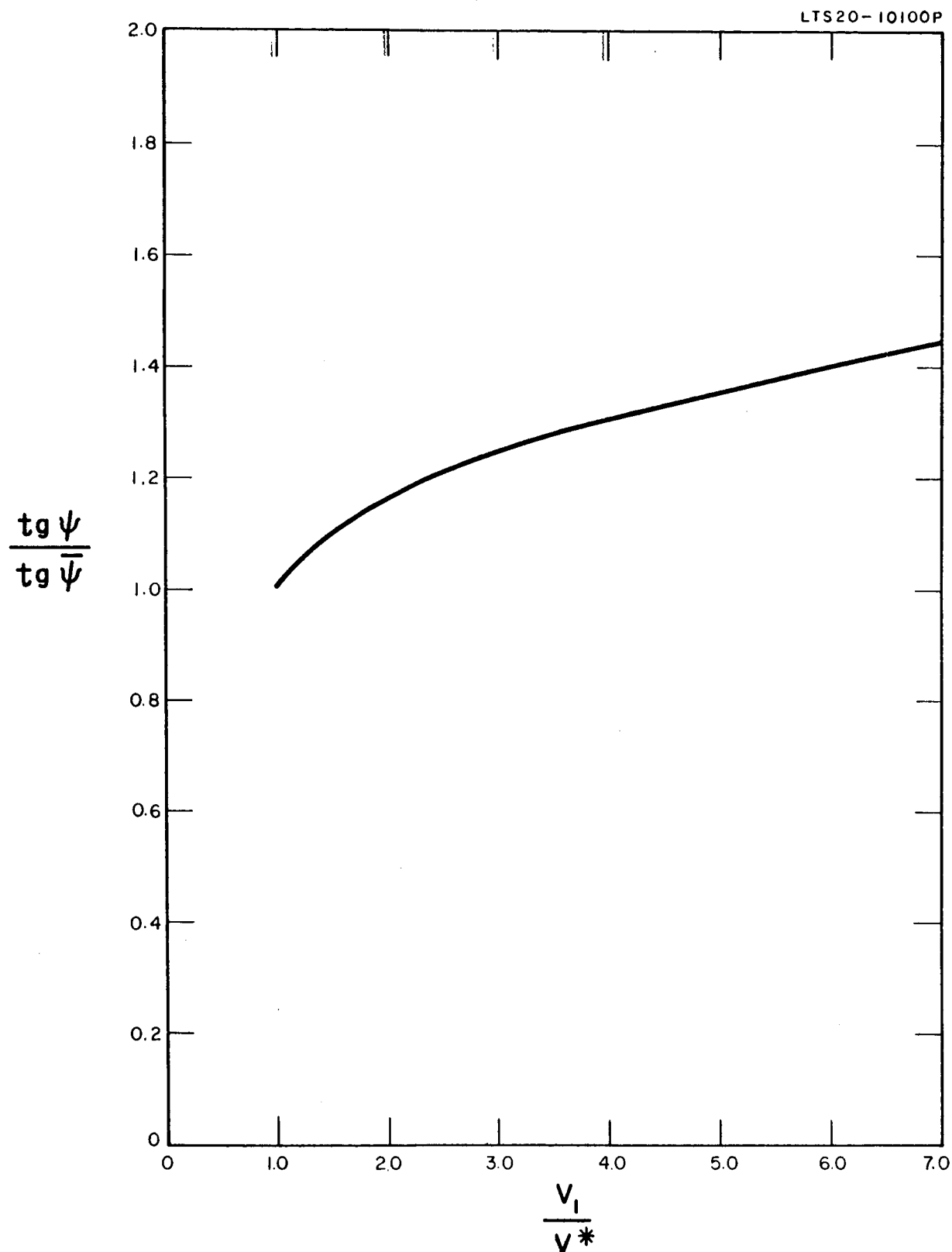
Figure 2-11. Energy dependence of magnetic deflection
(Test Model 1).

LTS18 - 1870P
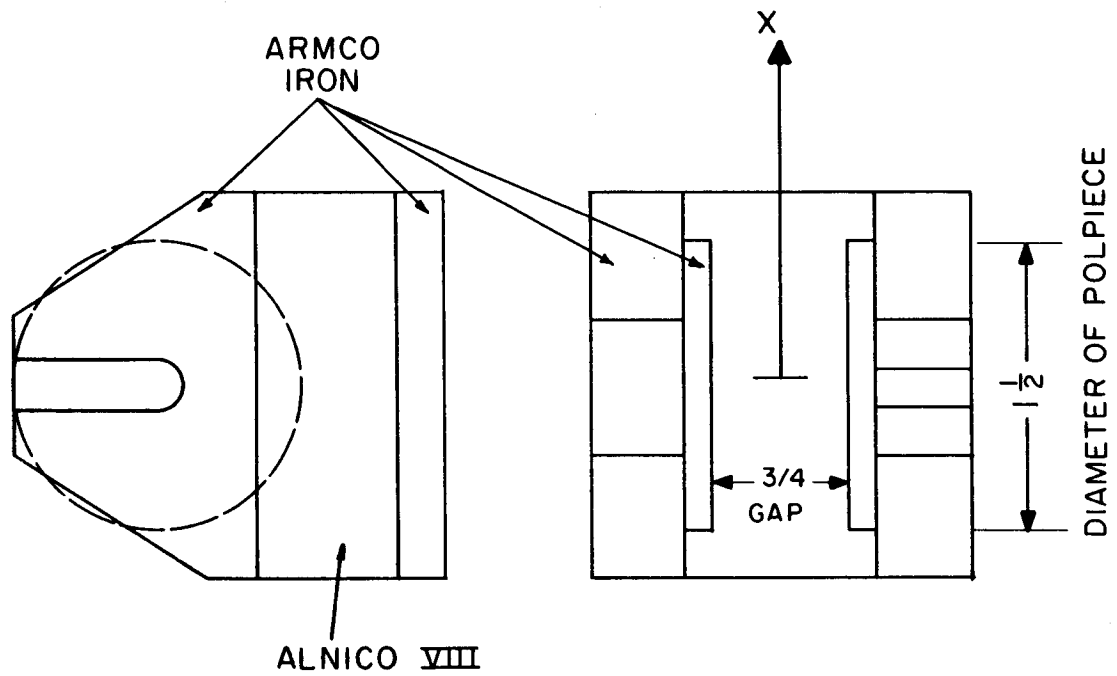
Figure 3-1. Magnet assembly for Test Model 1.

65
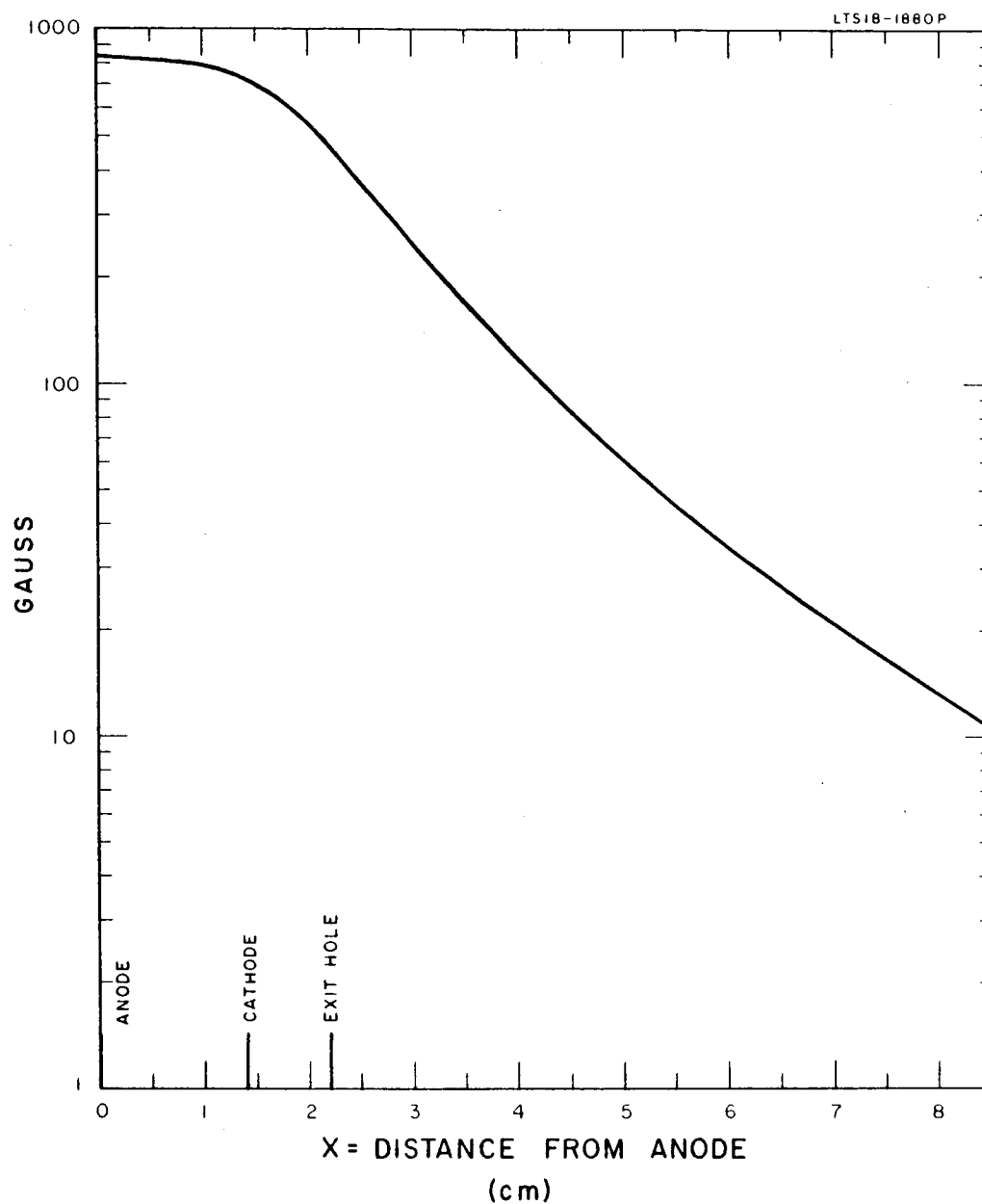
Figure 3-2. Magnetic field distribution of Model 1.
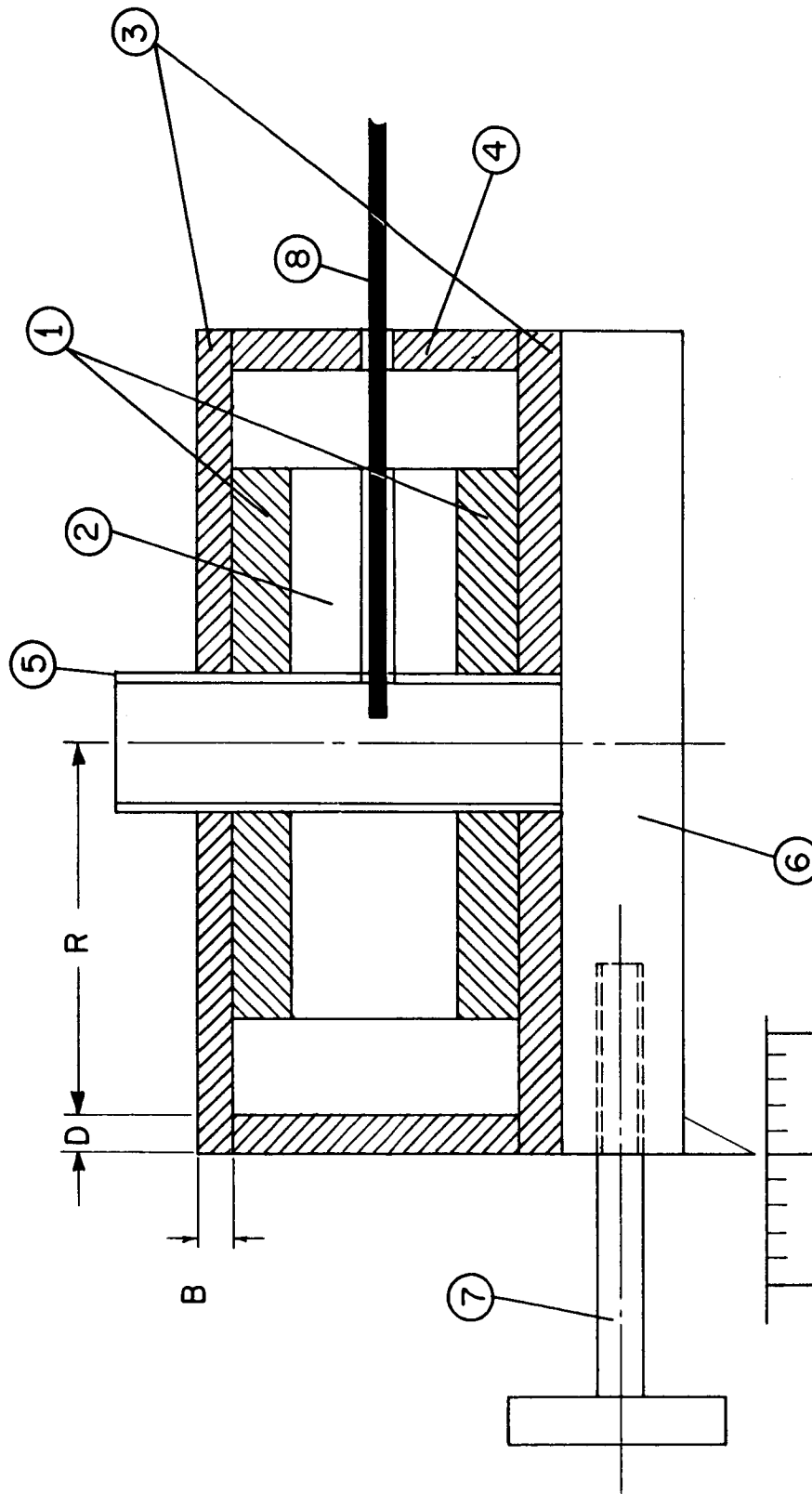
Figure 3-3. Magnet assembly for testing yoke dimensions.
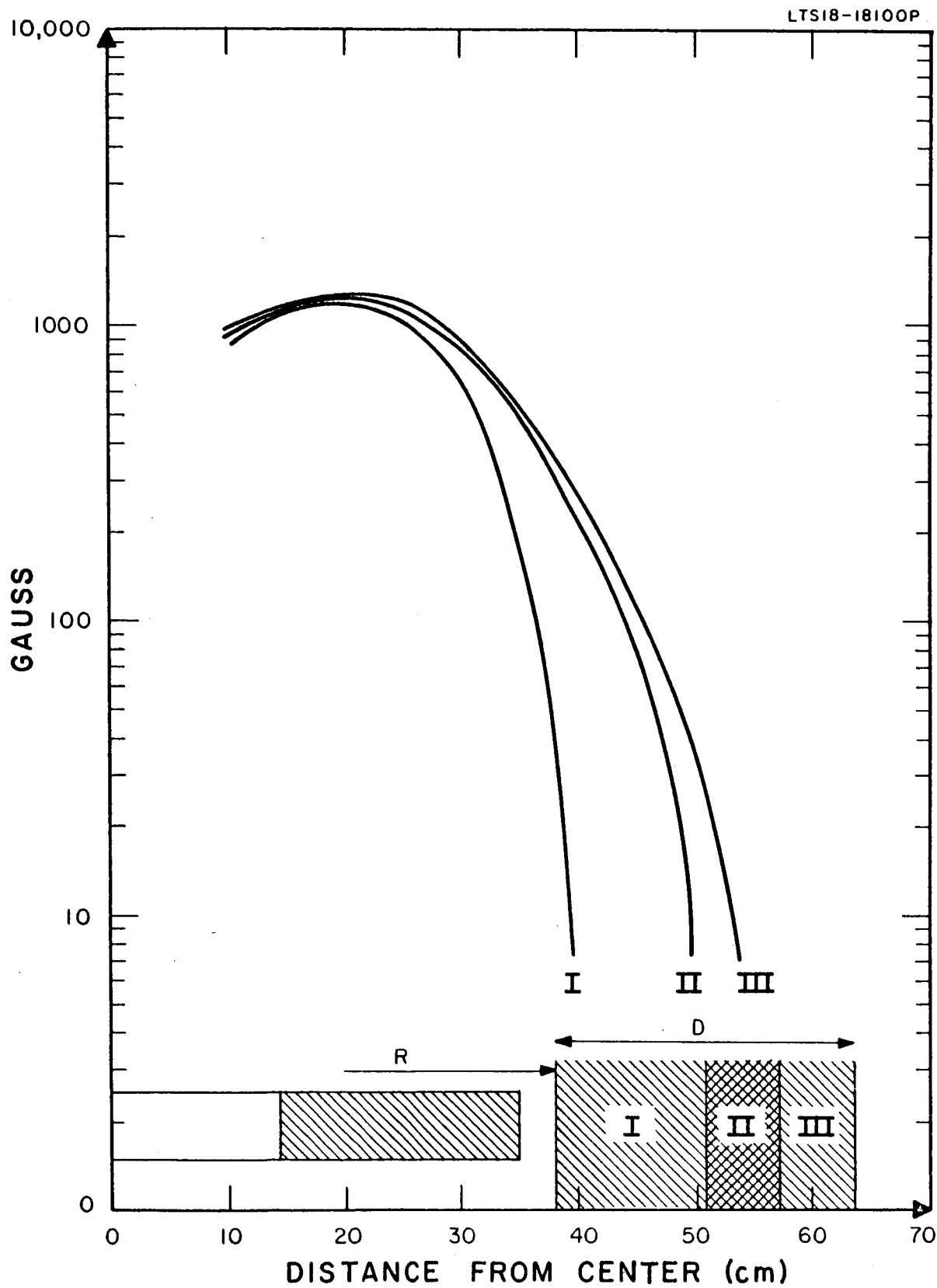
Figure 3-4. Field for different yoke dimensions.
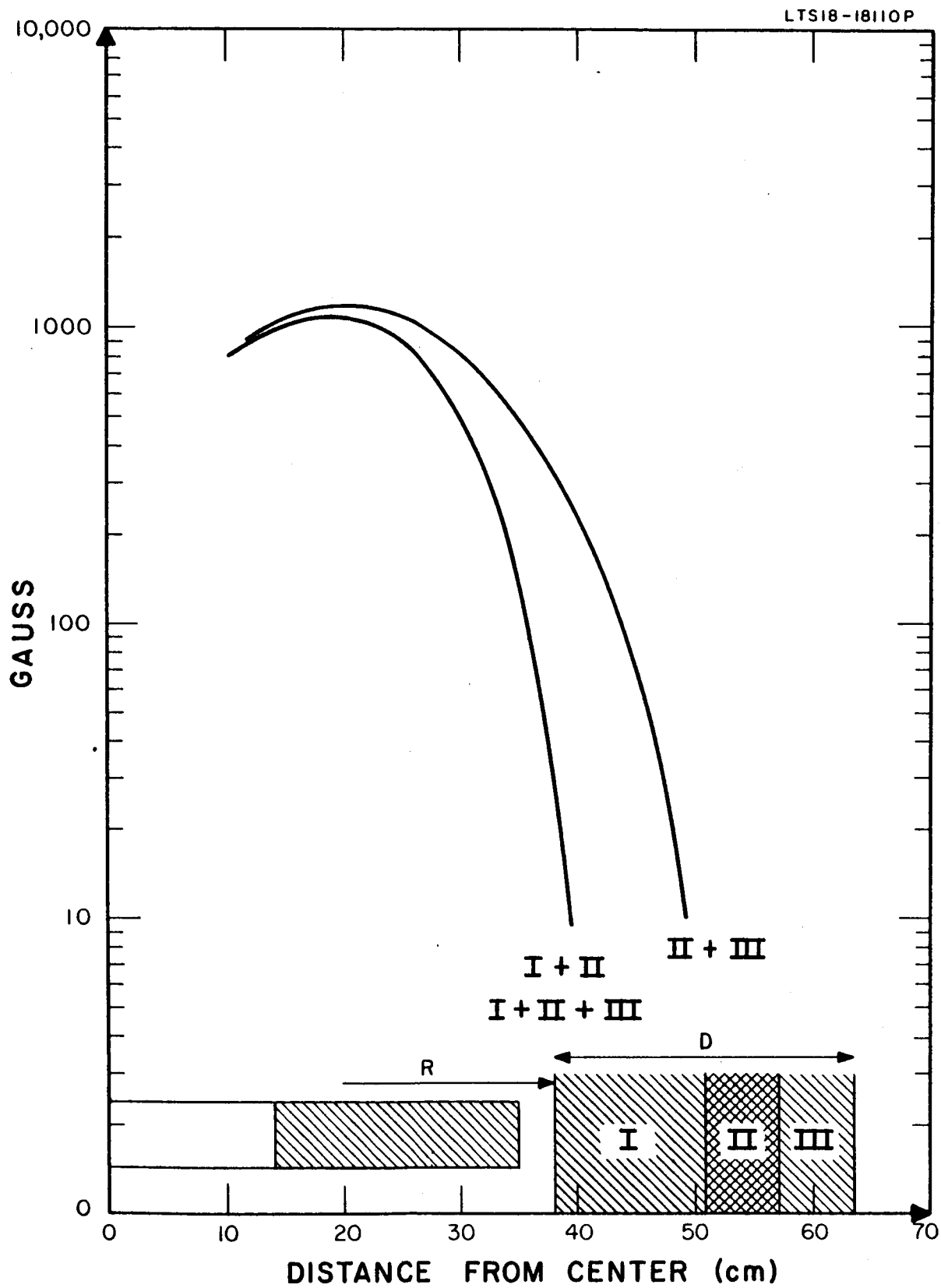
Figure 3-5. Field for different yoke dimensions.
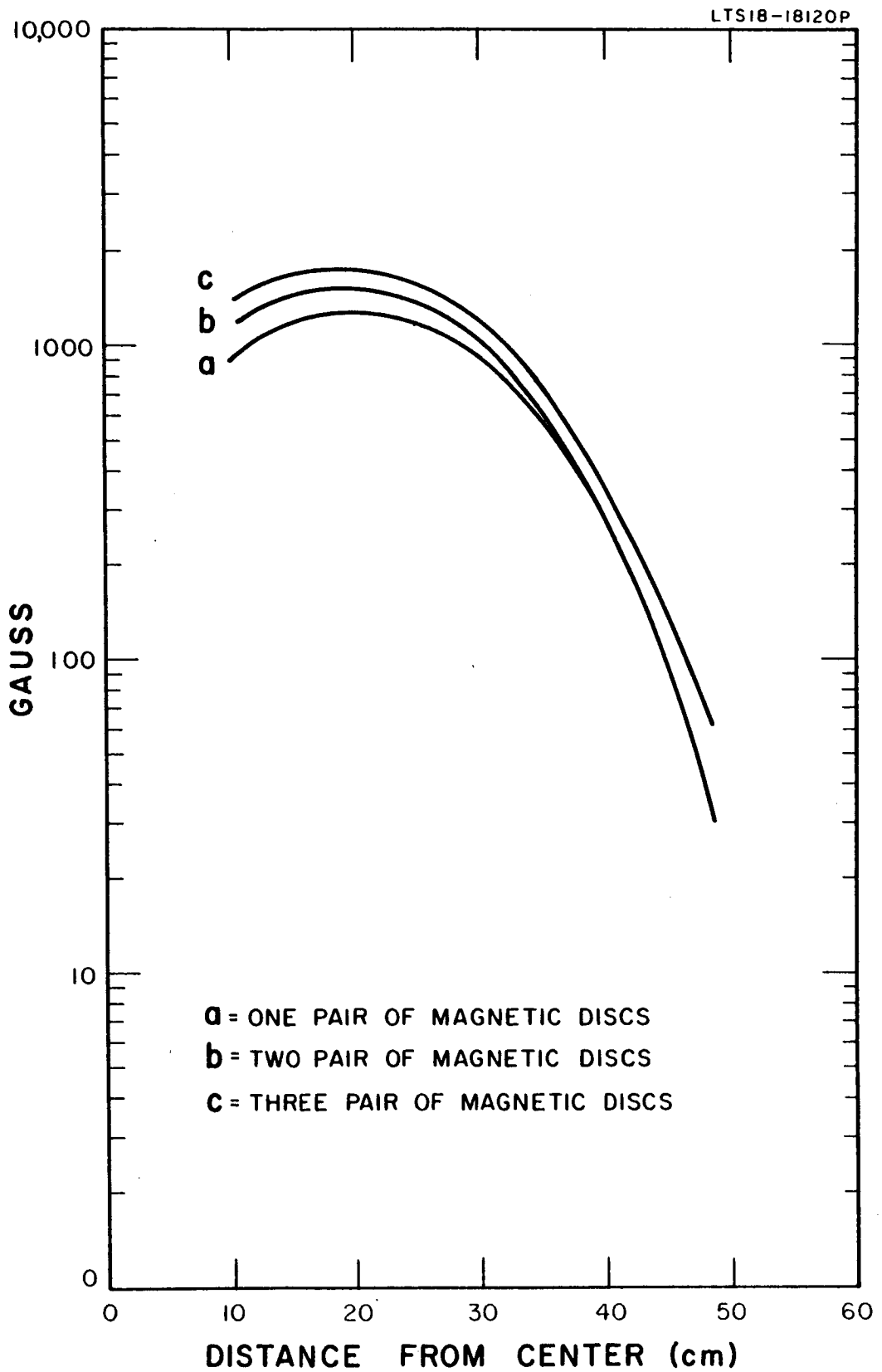
Figure 3-6.   Field for different thickness of magnetic material.
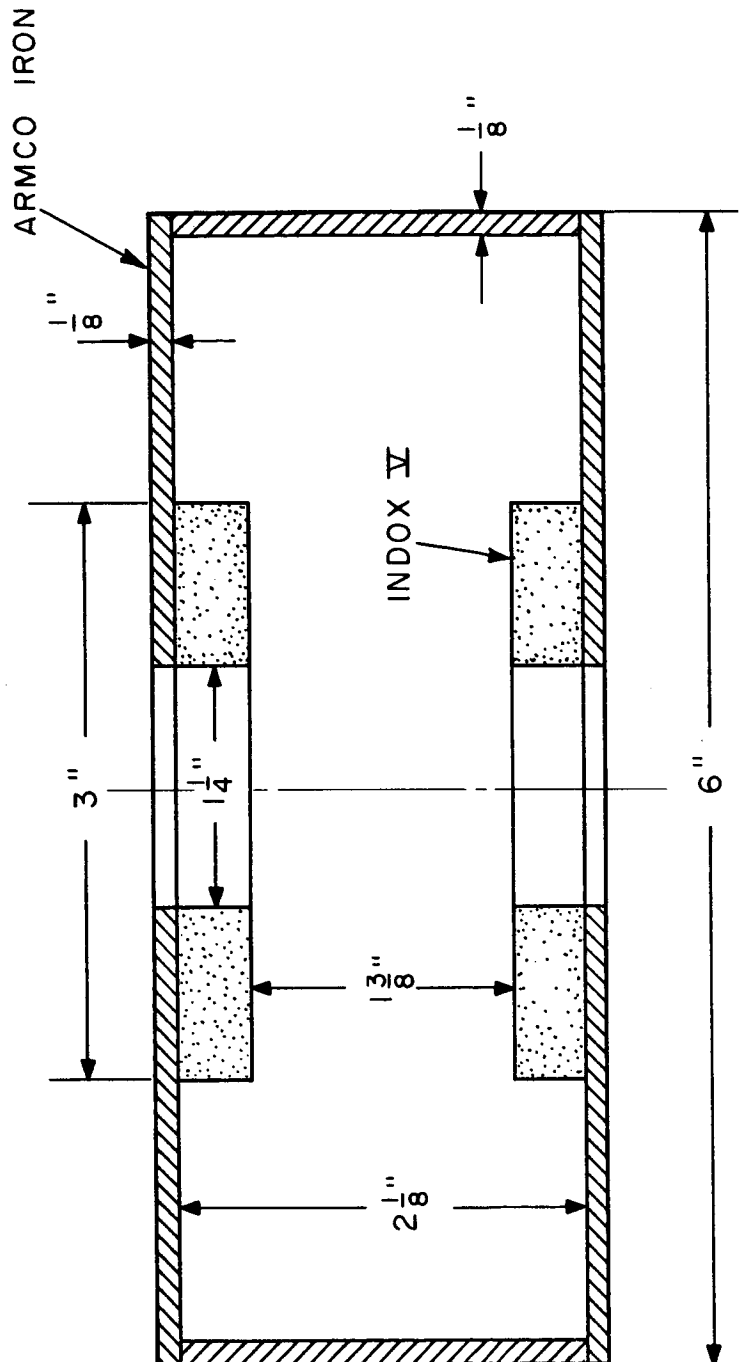
Figure 3-7. Magnet assembly for Test Model 2.

71
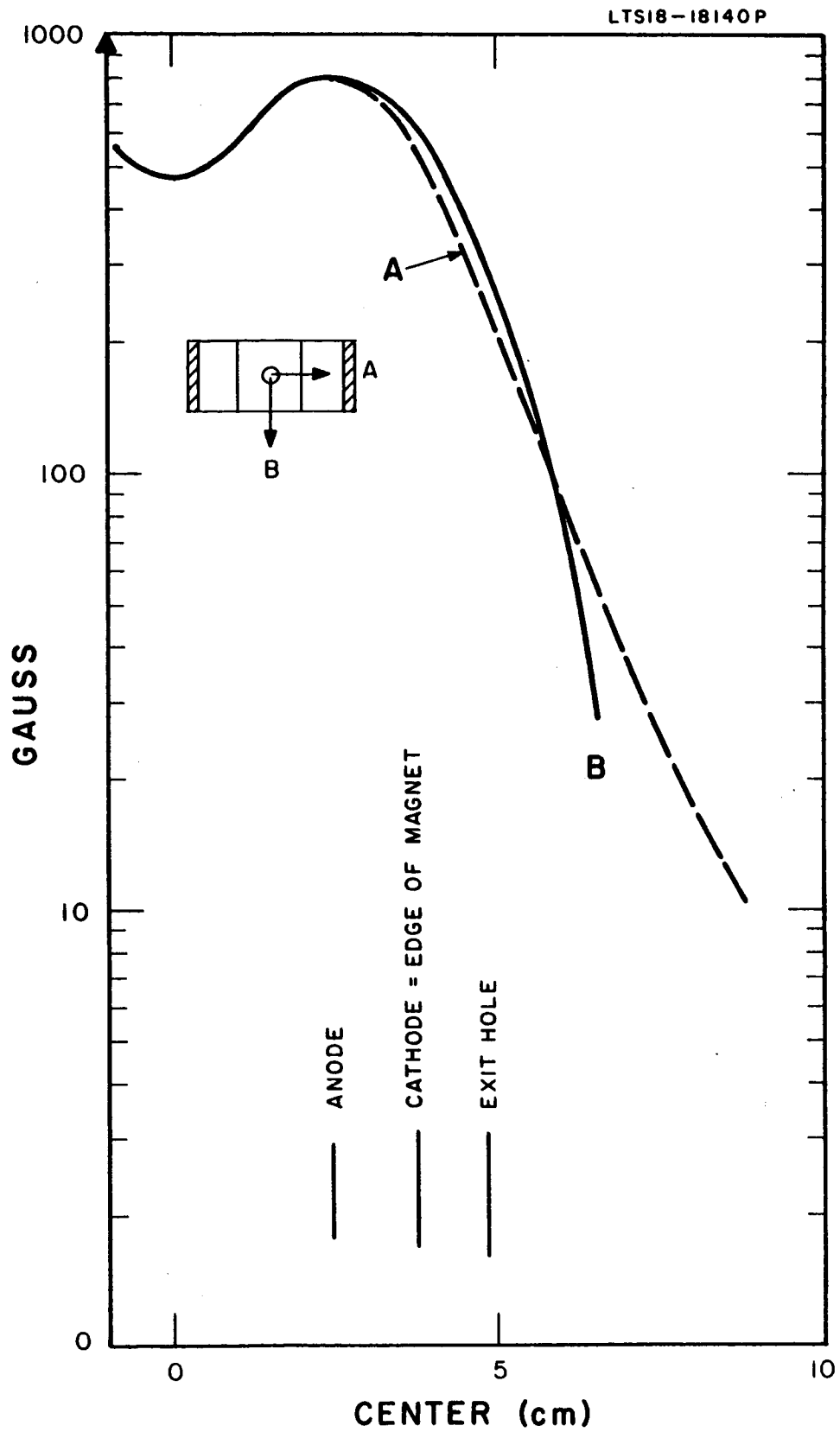
Figure 3-8. Magnetic field distribution of Test Model 2.

LTS18-18150P
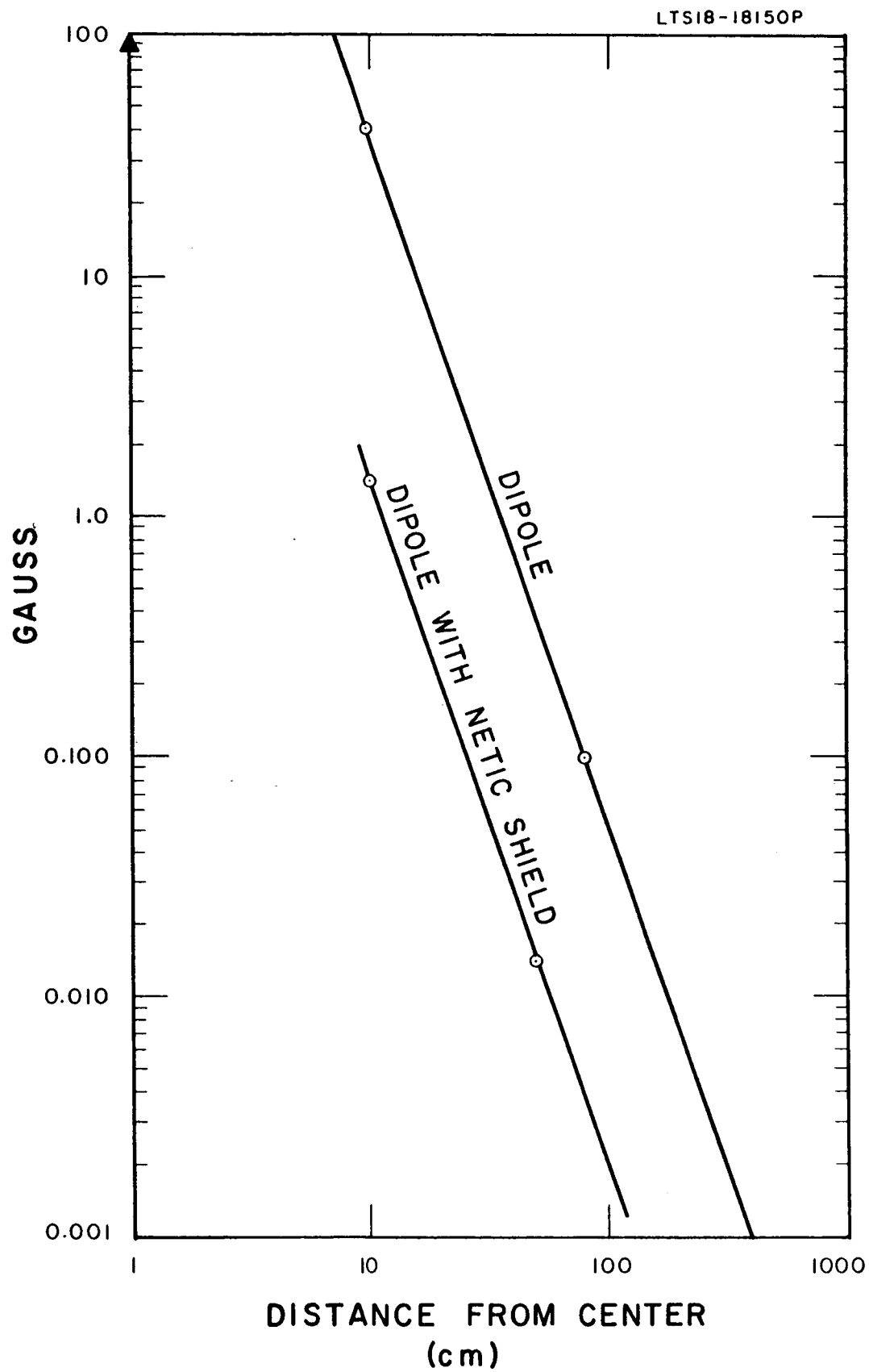
Figure 3-9. Fringe field of a dipole without and with shield.

73
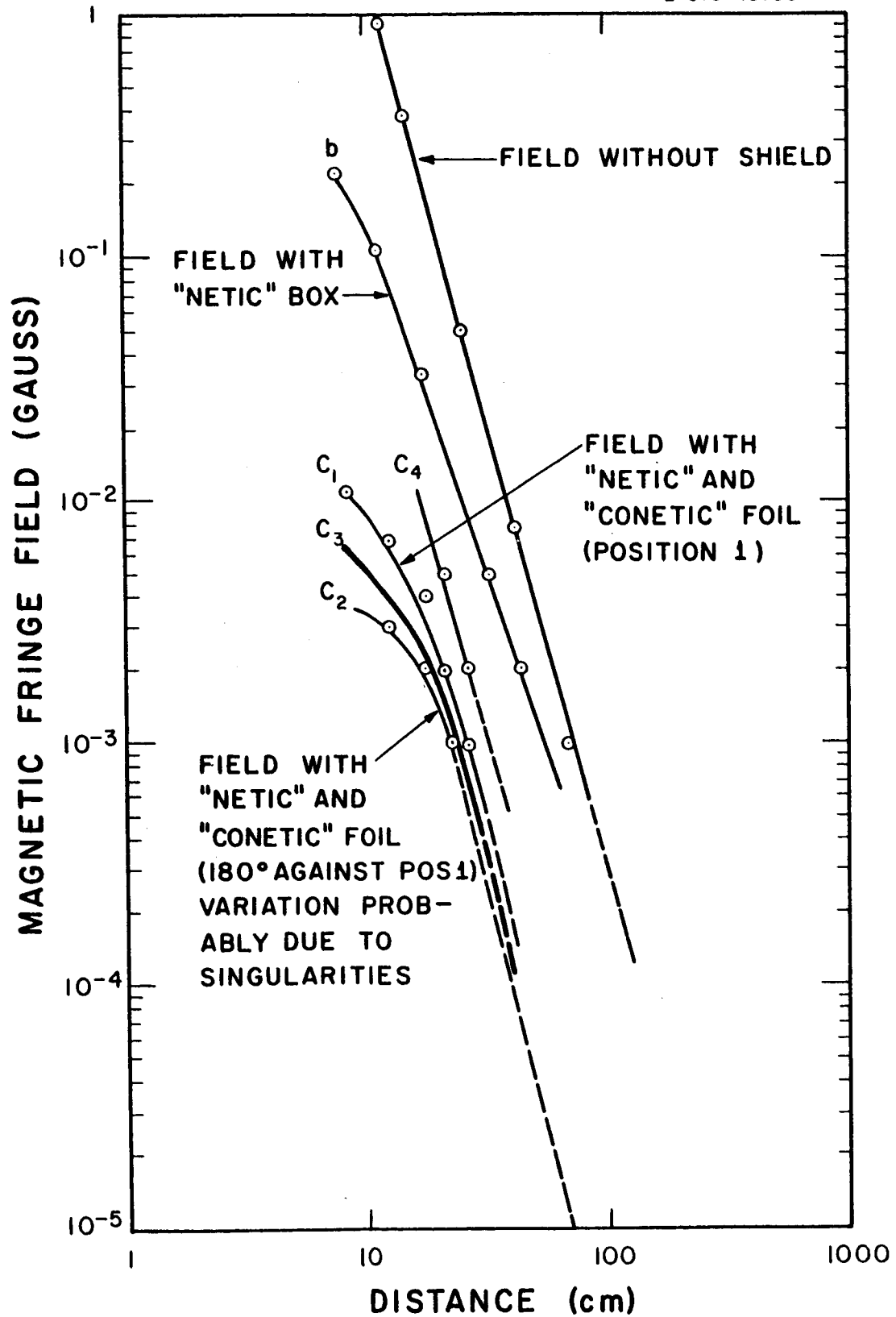
Figure 3-10. Fringe field of the magnet assembly for Test Model 2
without and with different shields.

LTSI8-I8I70P
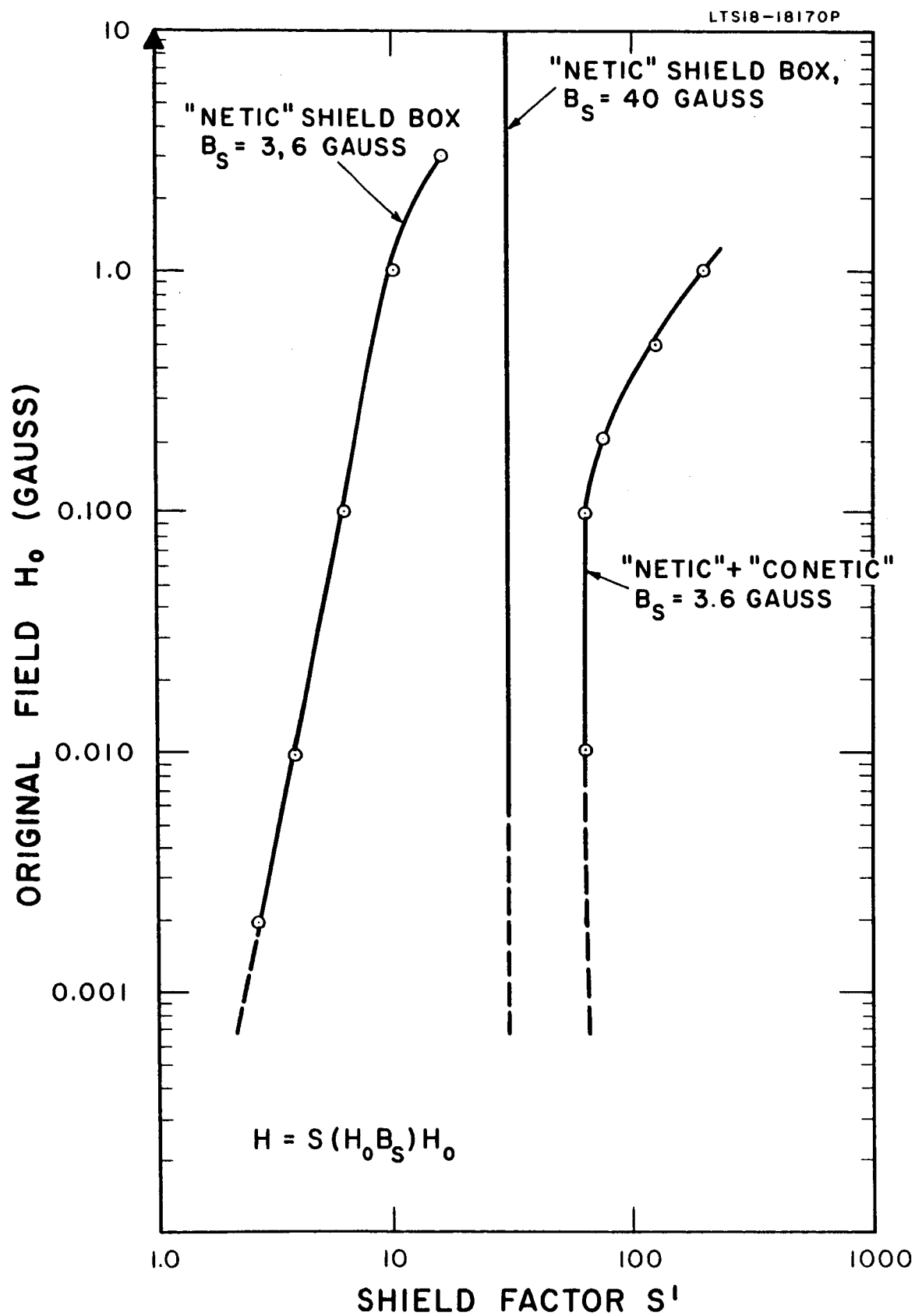
Figure 3-11.   Shield factor of different shield materials.

LTS18-18180A

Figure 4-1.   Schematic cross section of Test Model 1.
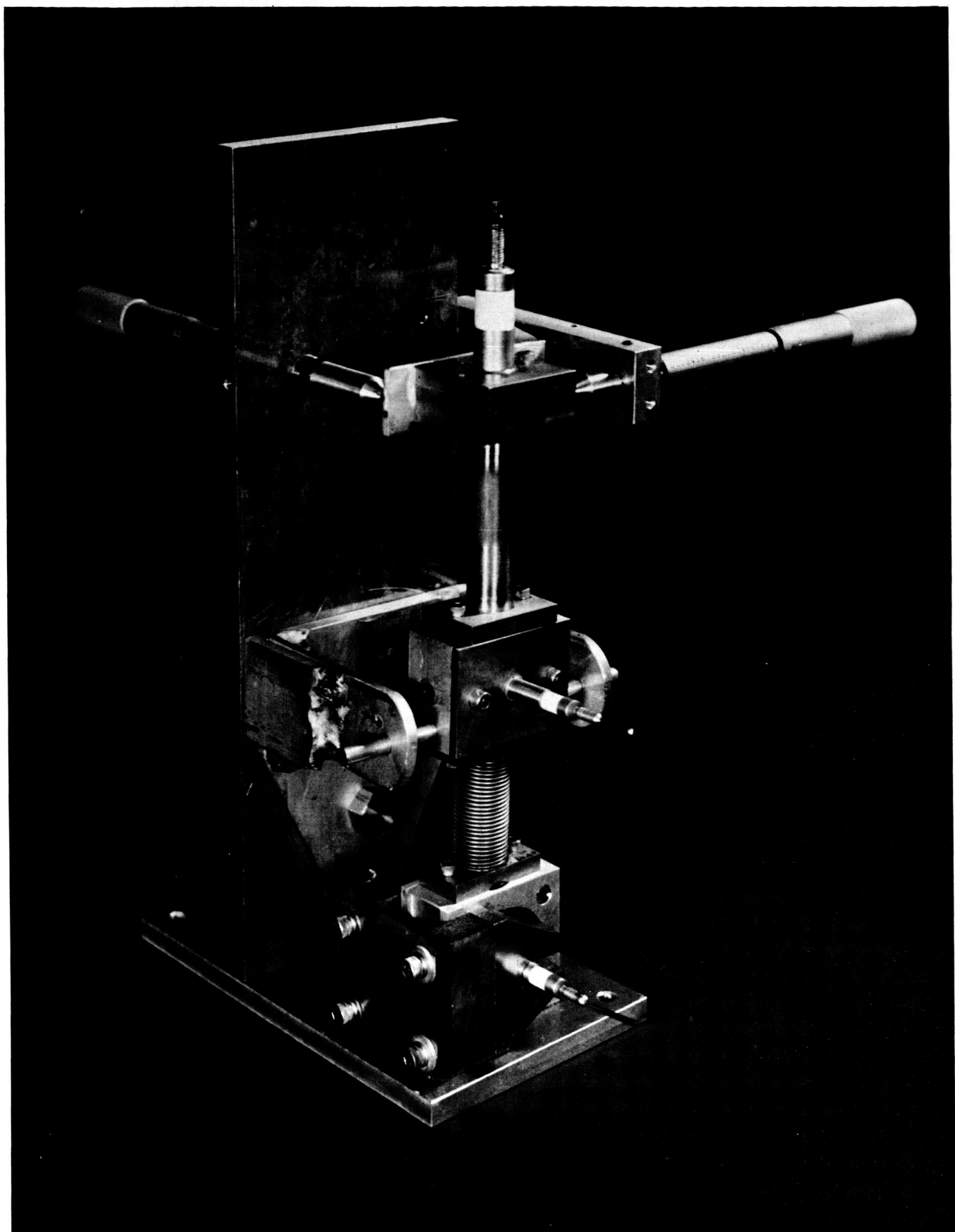
Figure 4-2. Photograph of Test Model 1.

77

LTS20-1050P

BACKGROUND GAS
PRESSURE 3×10^{-5} TORR

ANODE VOLTAGE (kv)

2.5

2.0

1.5

1.0

0.5

0

were
The data ~~was~~ taken by
starting at 2.5 kv and
decreasing the voltage
by 100 v every 2 minutes

100   200   300

DISCHARGE CURRENT (μA)
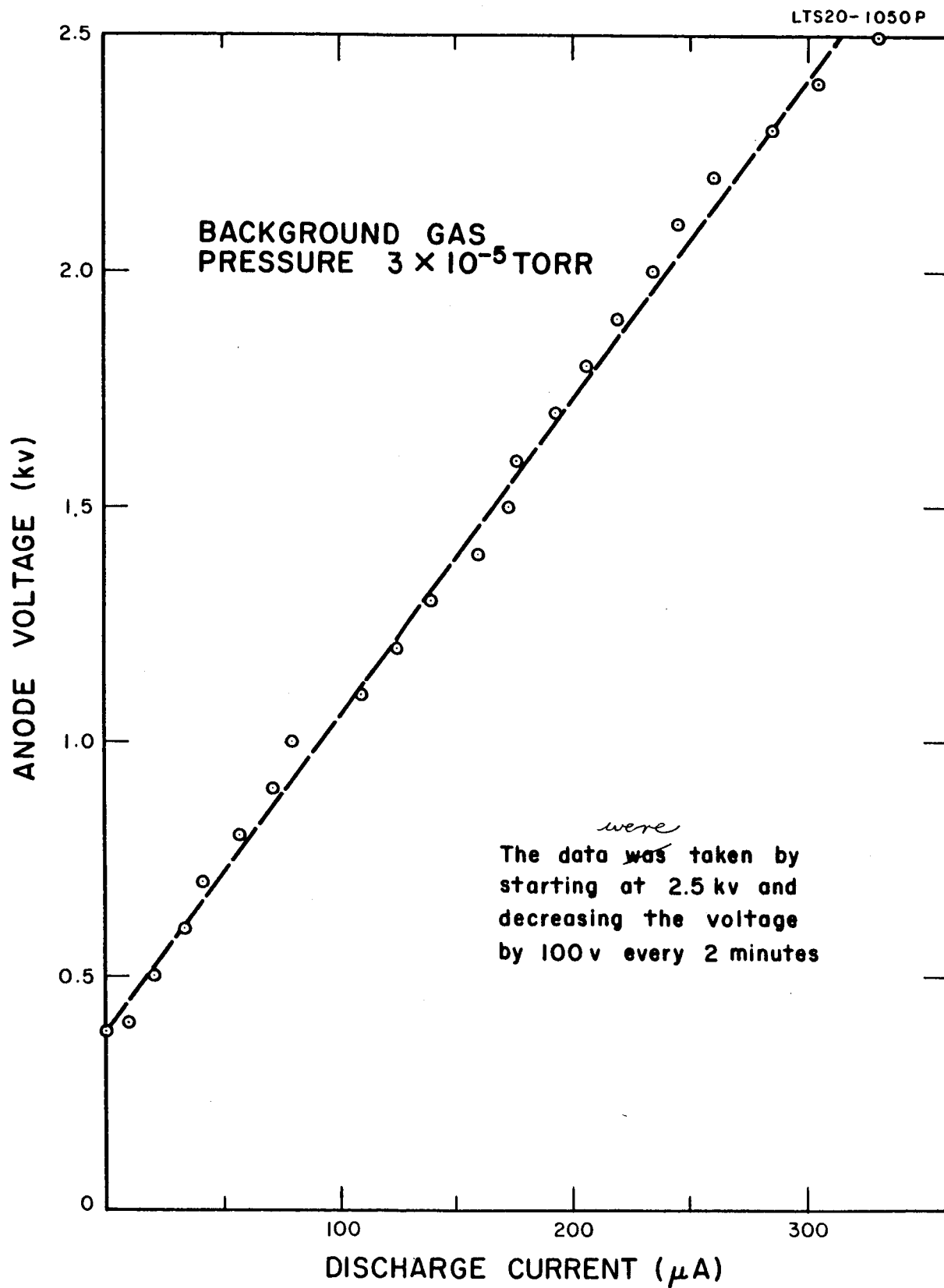
5-1.   Current-voltage characteristic of the discharge of
Model 1 with round anode.

Figure 5-2. Mass spectrograms of different gases and vapors. Linear current scale. Ion gauge readings of equivalent air pressure. Discharge voltage 1500 volts.
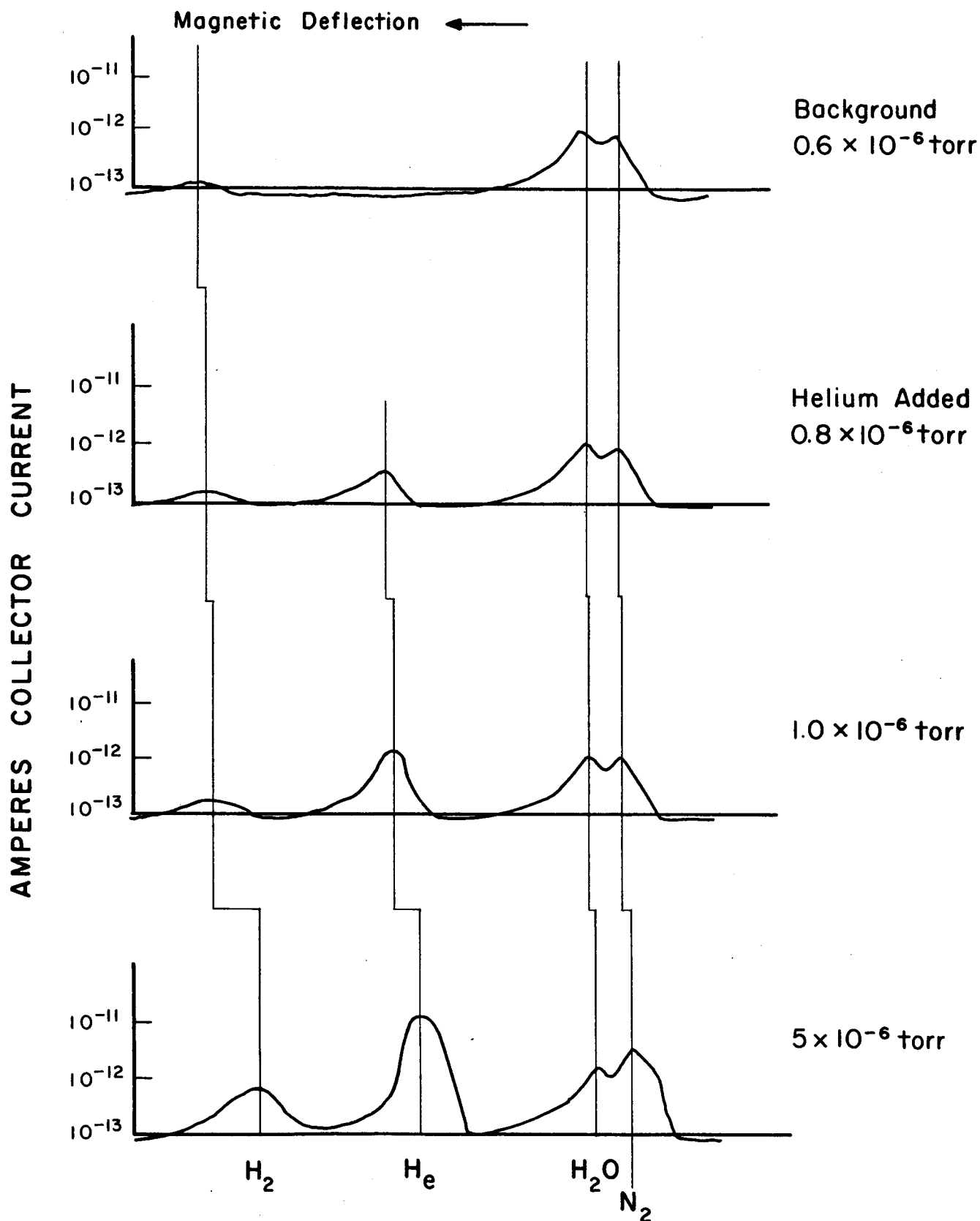
Figure 5-3. Pressure dependence of peak positions.
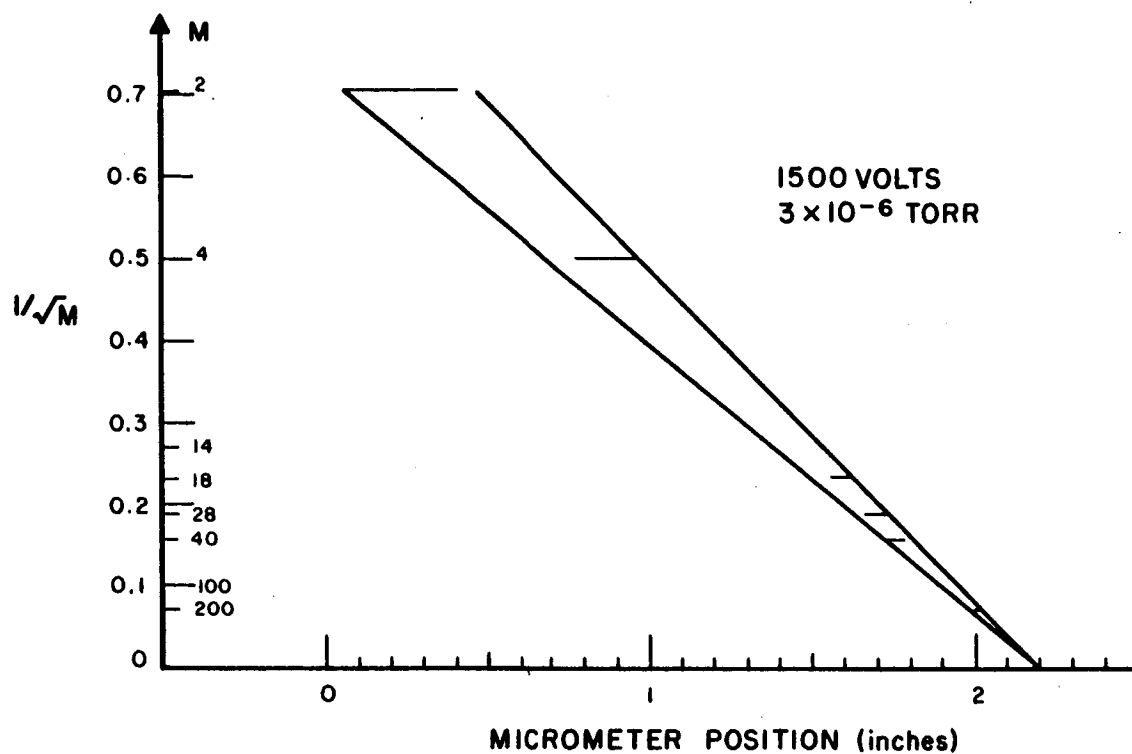
Figure 5-4. Experimental mass scale.
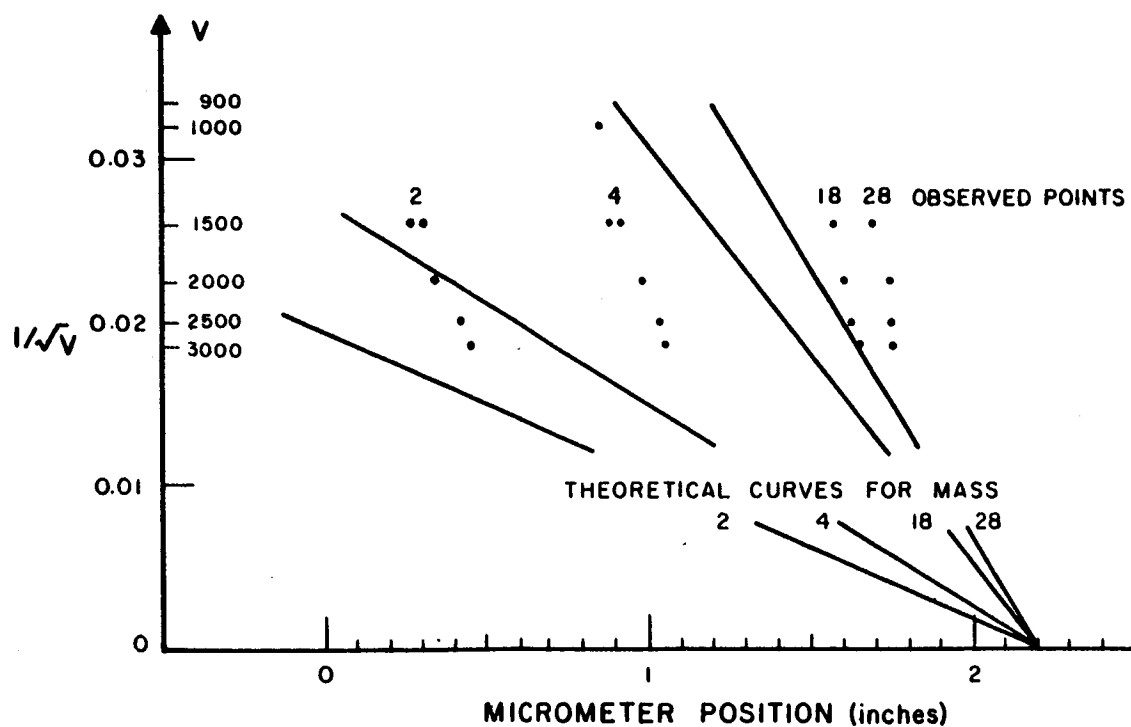
Figure 5-5. Theoretical and experimental peak positions as a function of the discharge voltage.

81
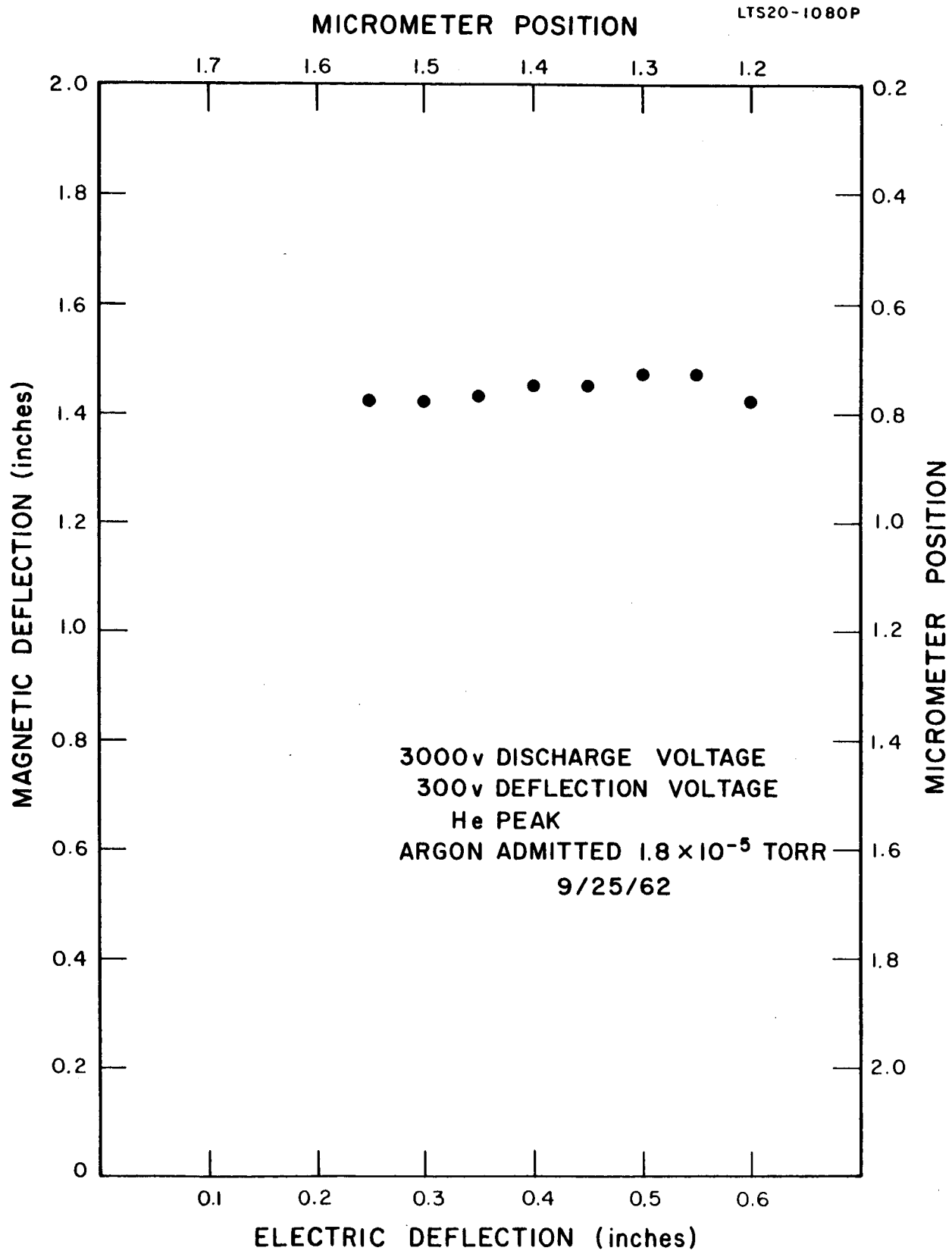
Figure 5-6. Experimental energy dependence of magnetic deflection for Test Model 1. Demonstration of velocity focusing.

LTS20—1090P
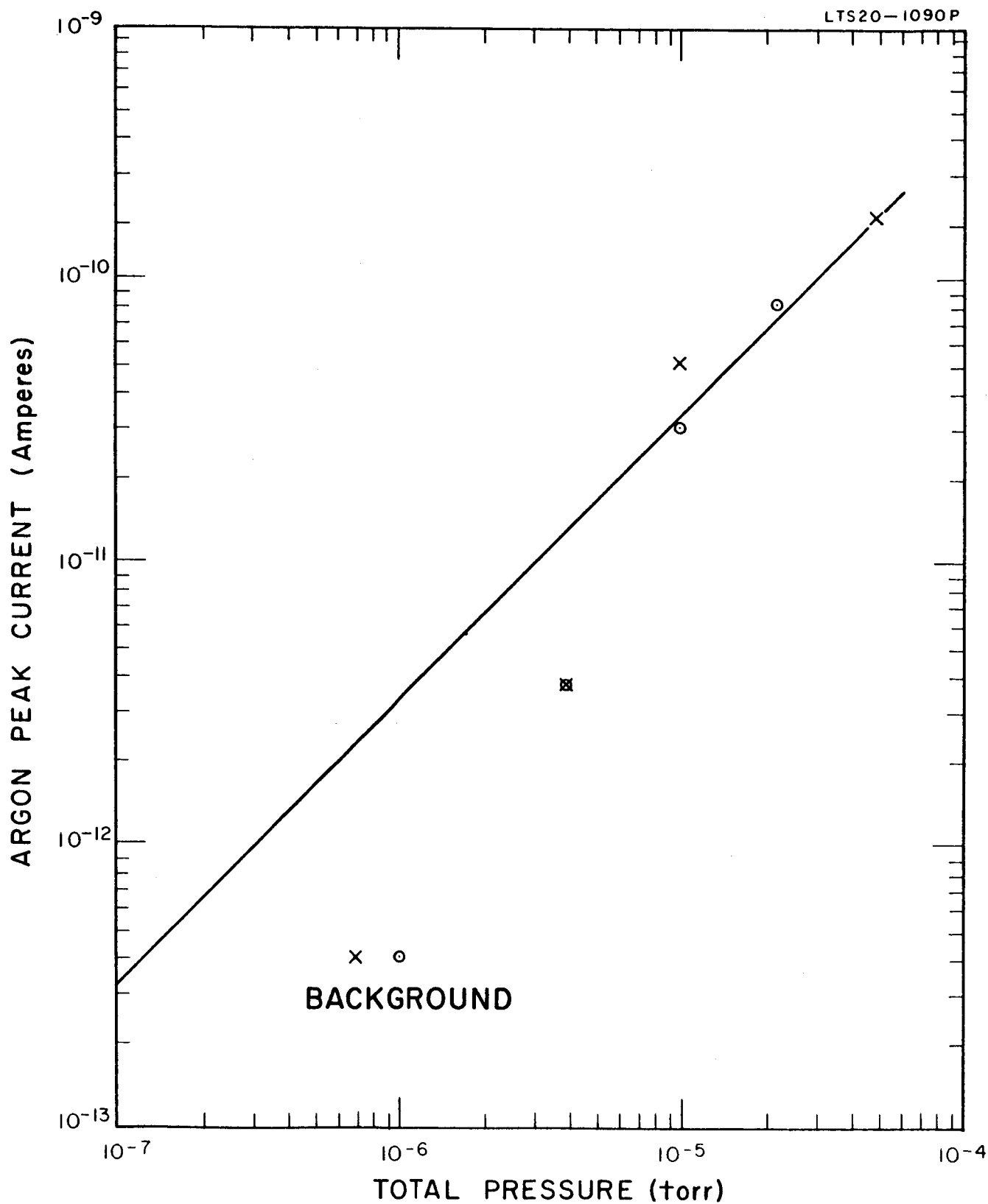
Figure 5-7.   Pressure dependence of peak height (Test Model 1).

6 10 5 9 11 12 13 6 6

Figure 6-1. Schematic cross section of Test Model 2.
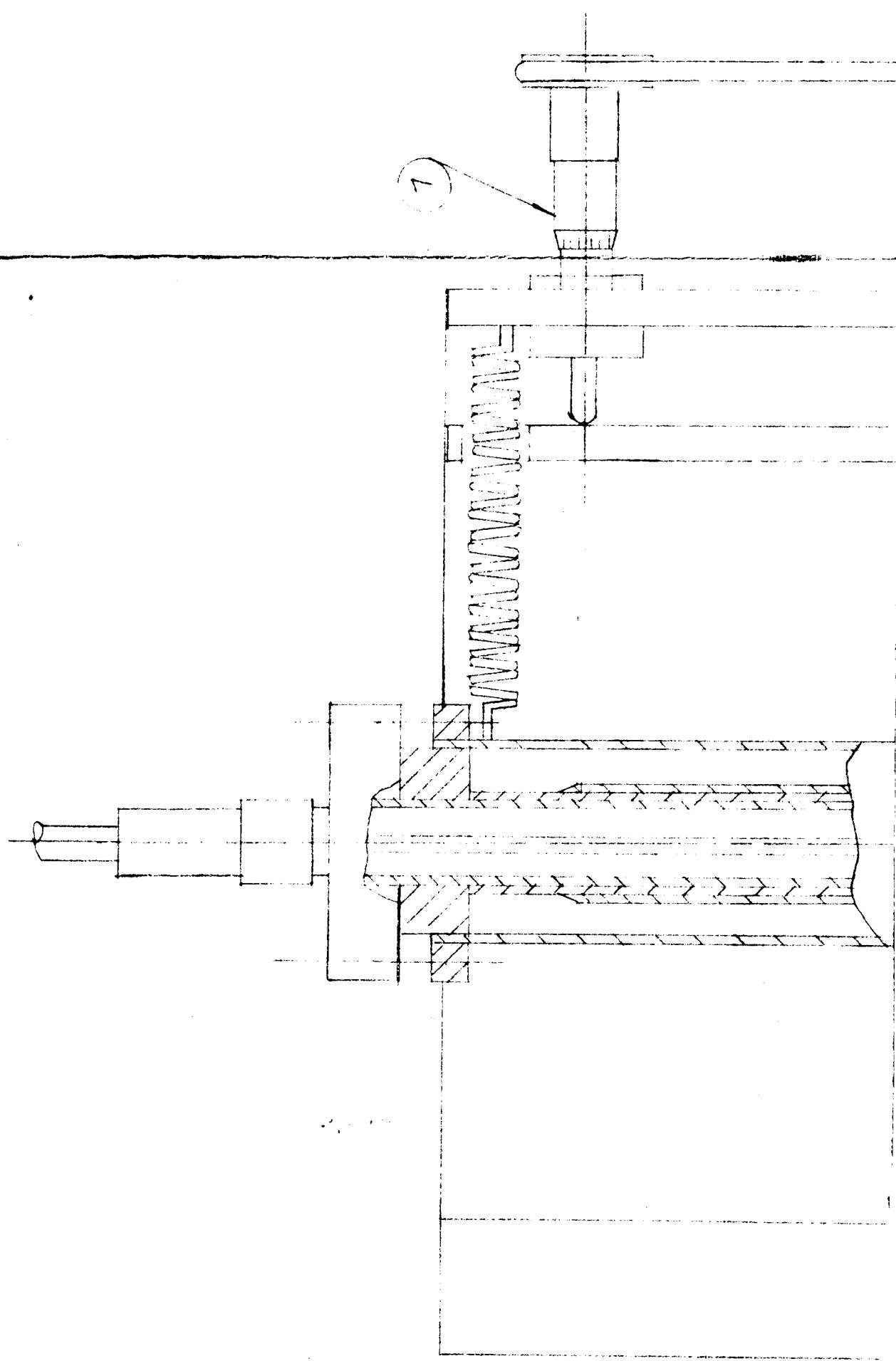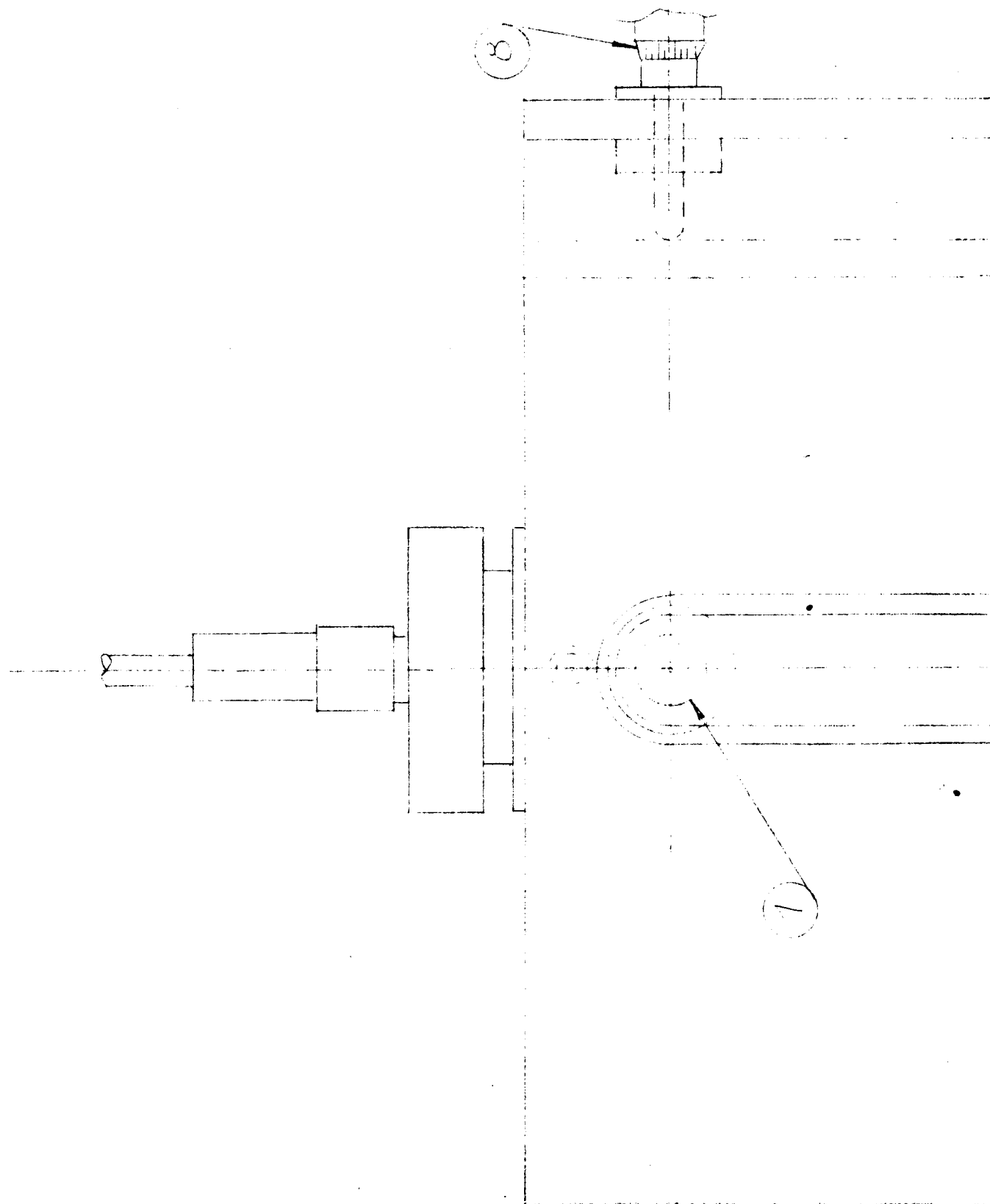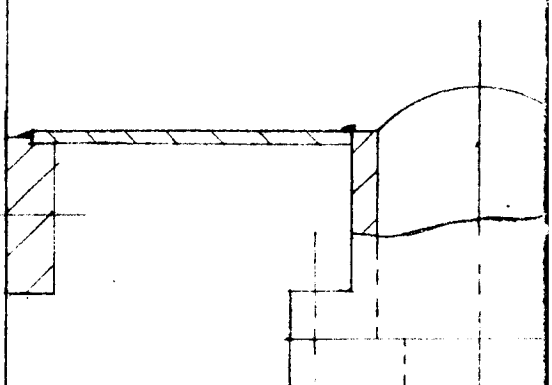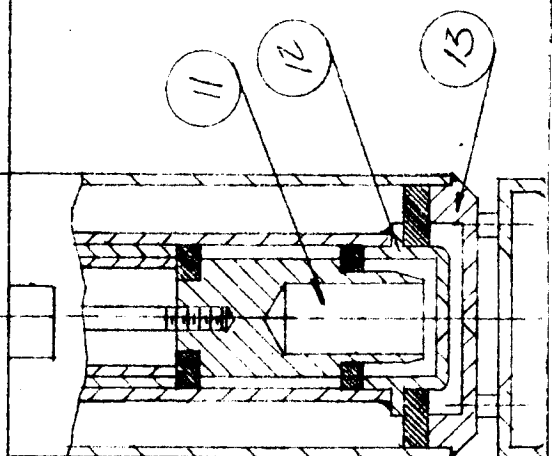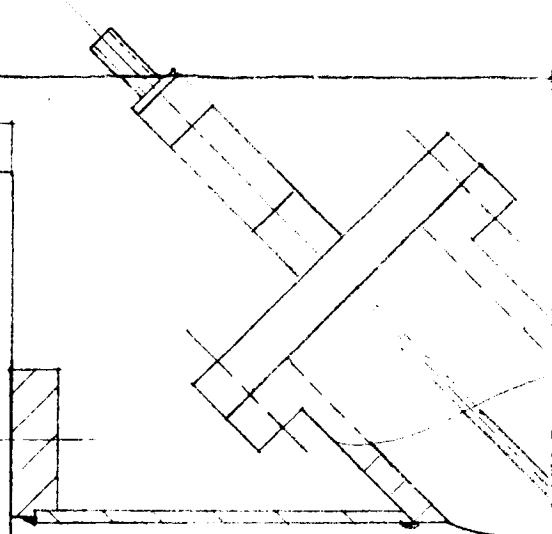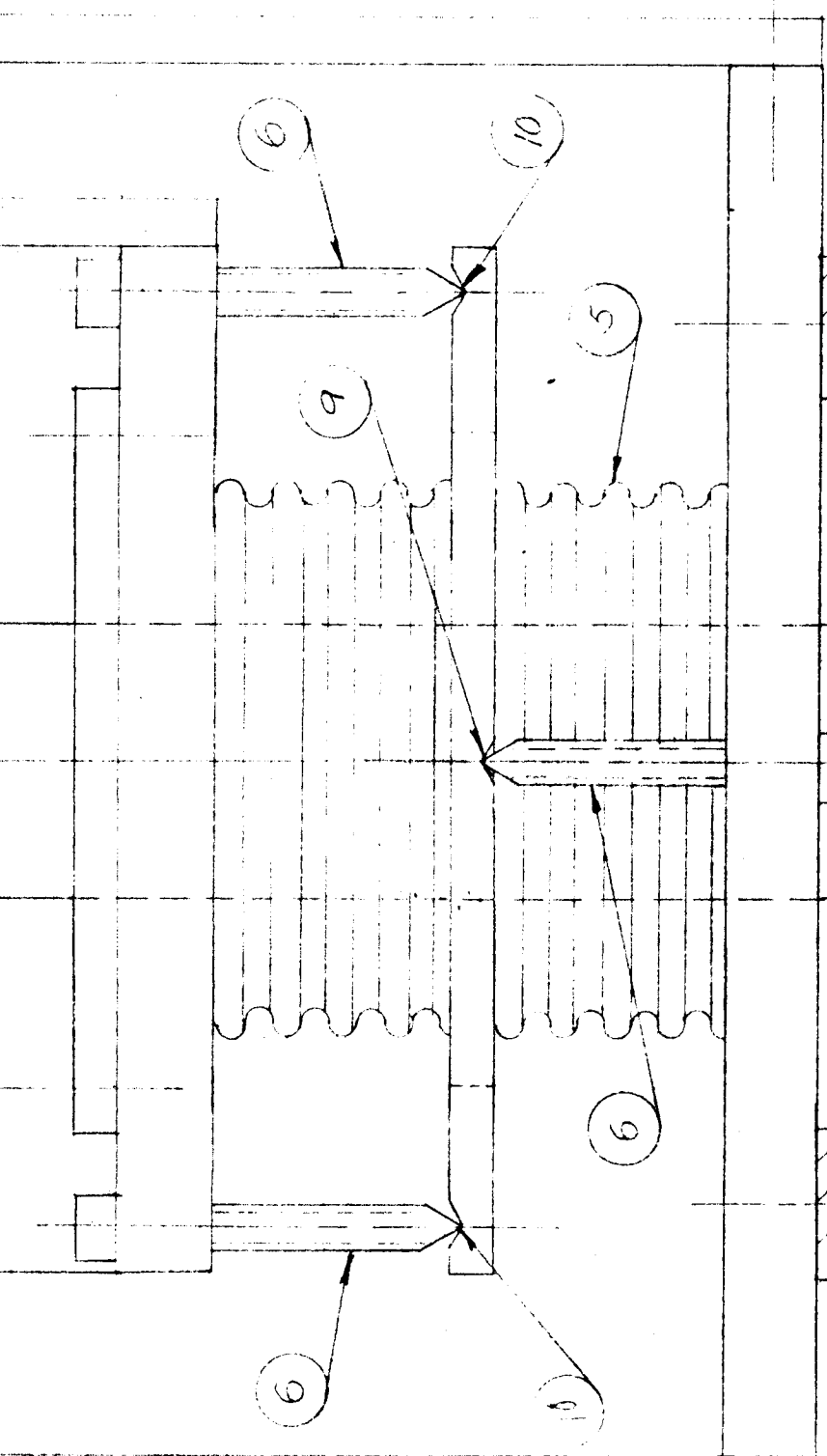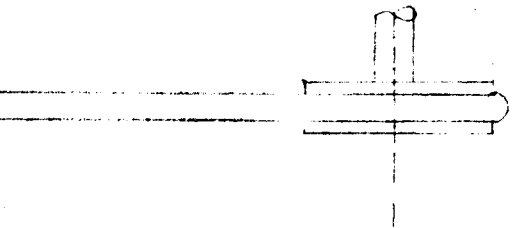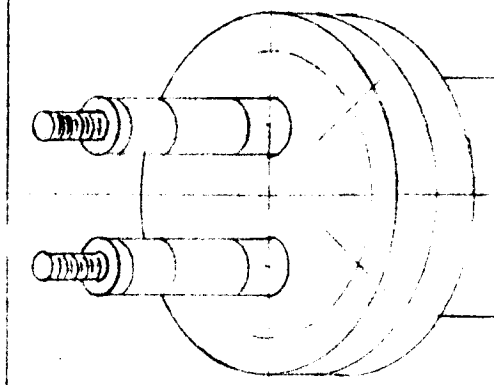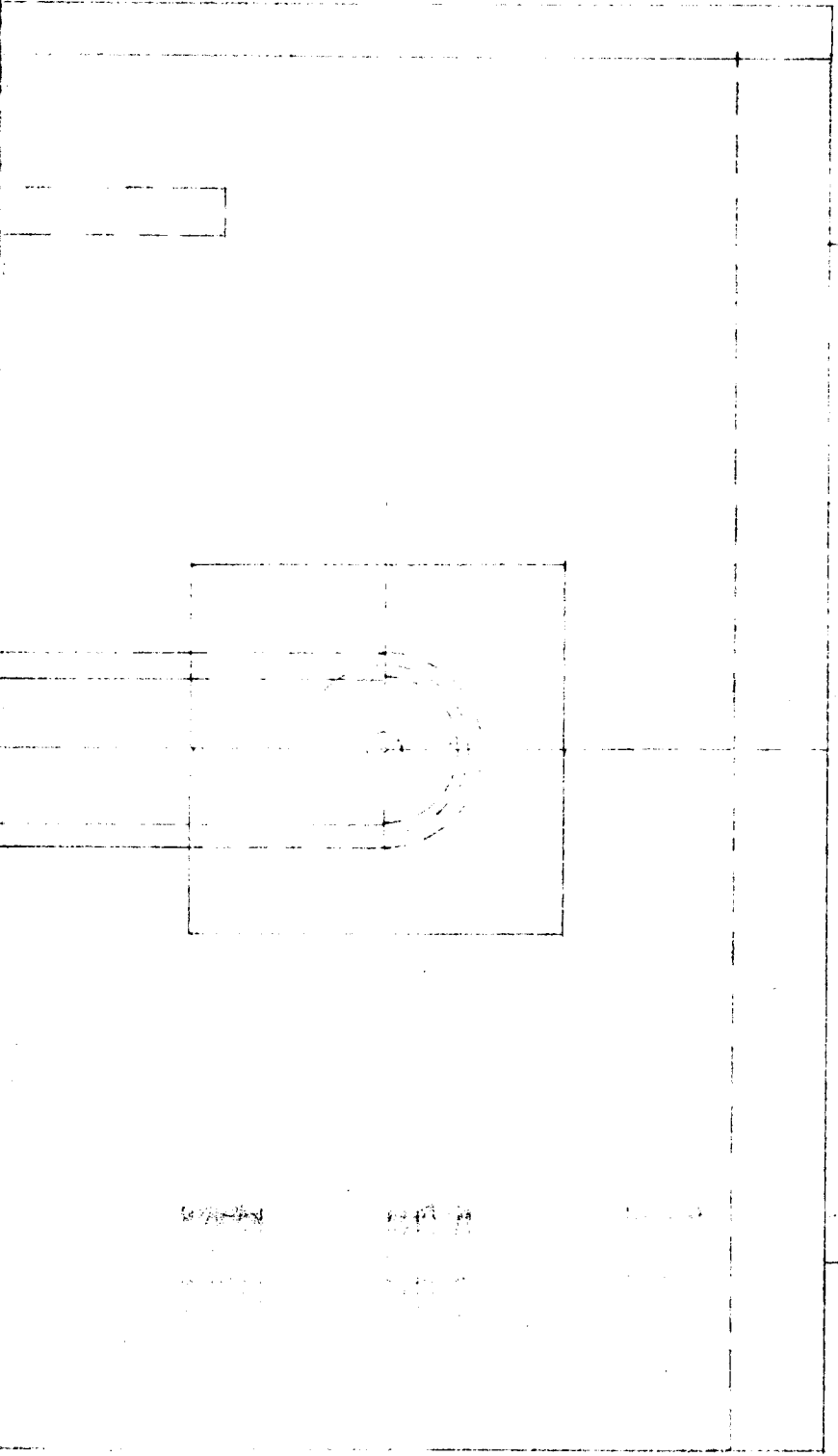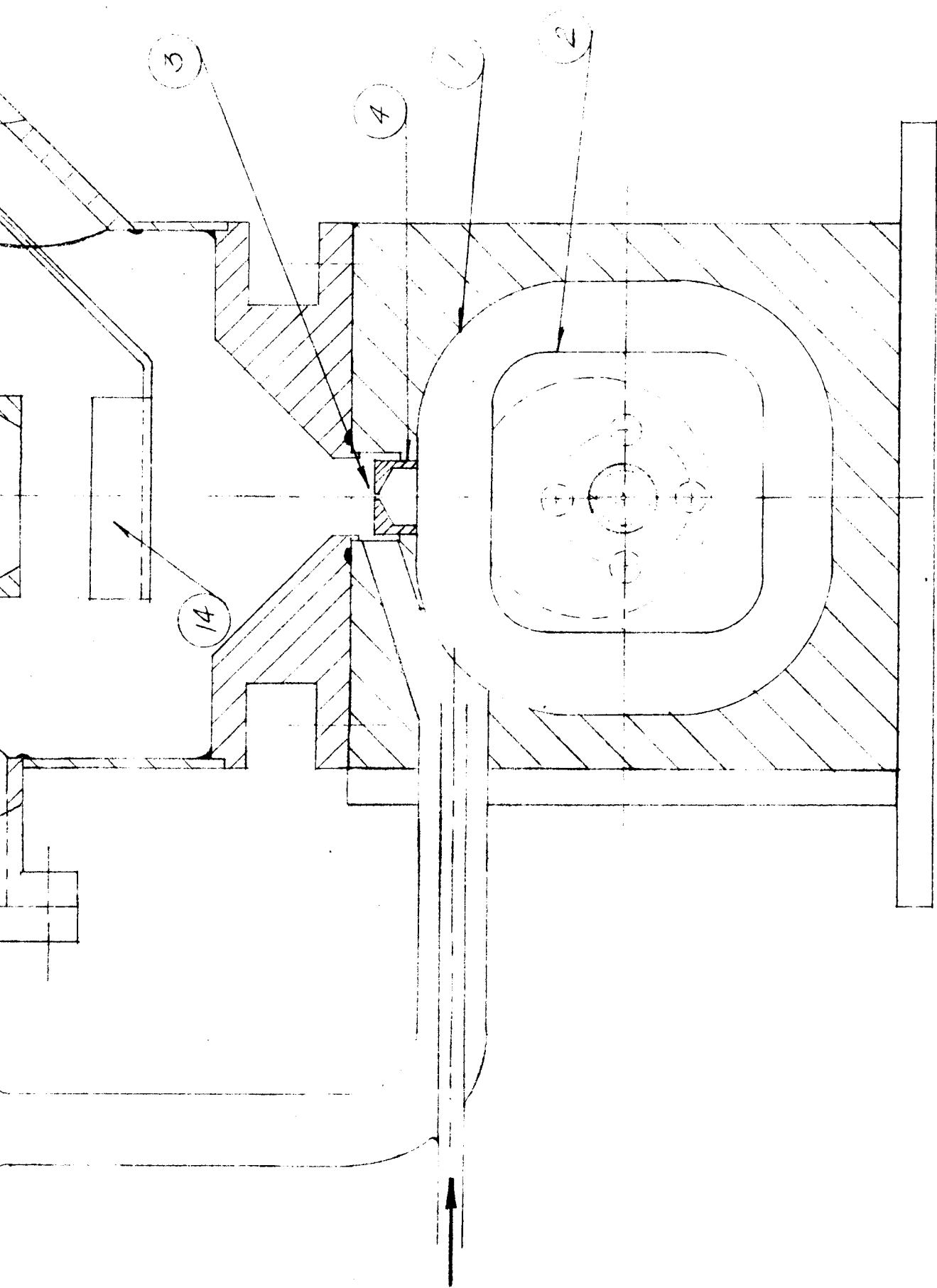
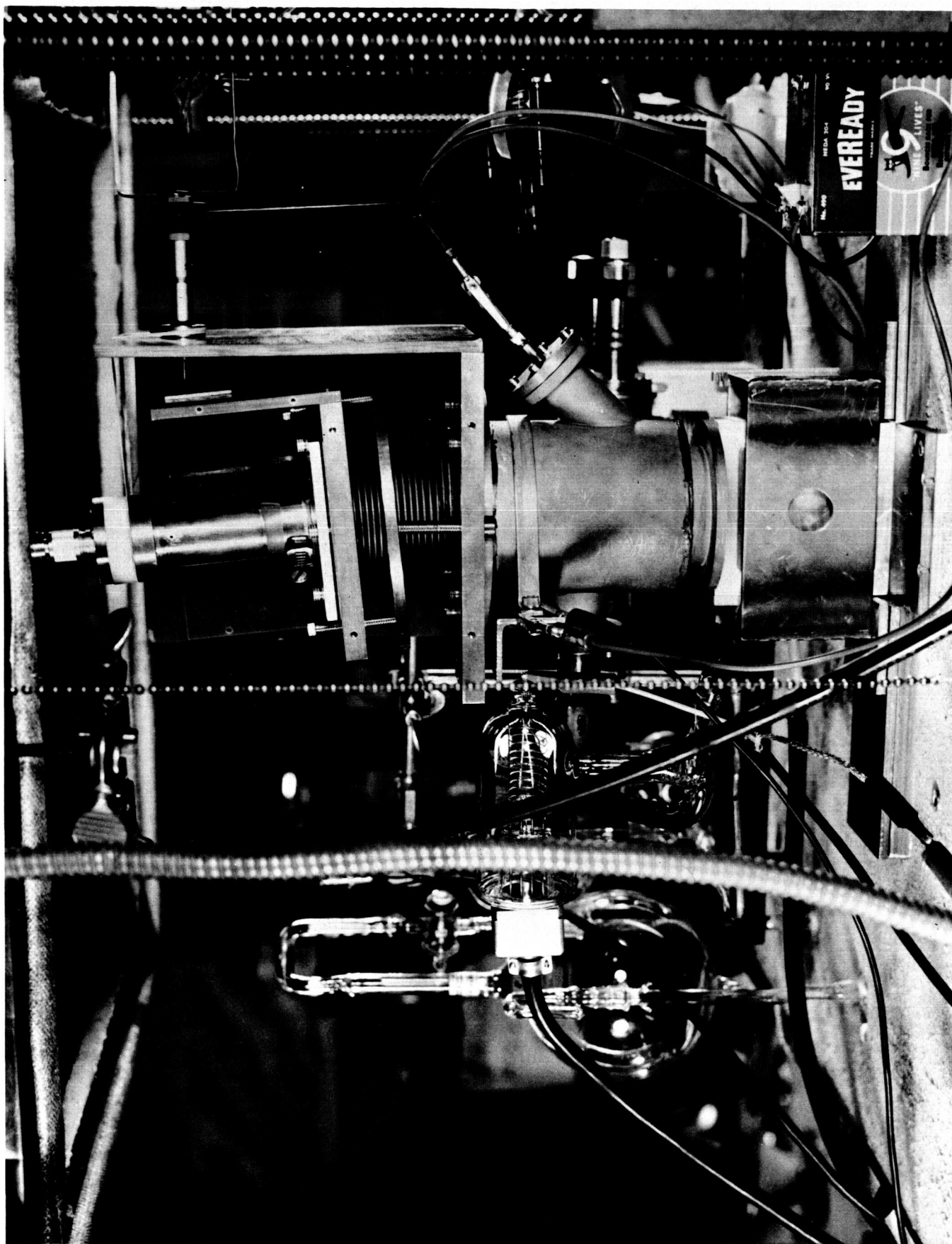FIGURE 6-1

TEST SYSTEM MODEL 2
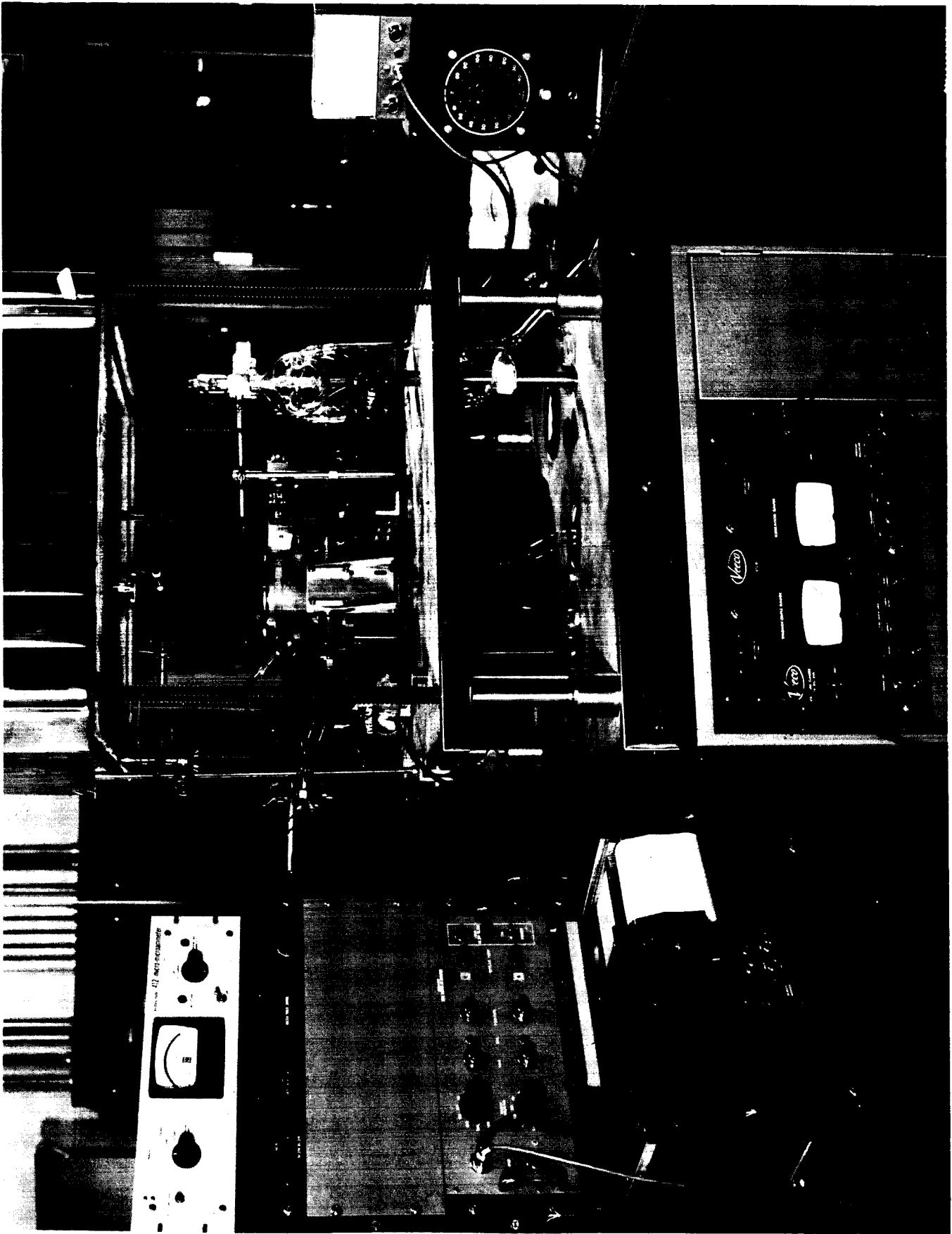
Figure 6-2. Photograph of Test Model 2 (closeup).

Figure 6-3. Photograph of Test Model 2 (overall setup).

86